



Multiscale analysis of a very long wind turbine wake in an atmospheric boundary layer

Fengshun Zhang , Xiaolei Yang ,* and Guowei He

*The State Key Laboratory of Nonlinear Mechanics, Institute of Mechanics,
Chinese Academy of Sciences, Beijing 100190, China*

and School of Engineering Sciences, University of Chinese Academy of Sciences, Beijing 100049, China



(Received 25 April 2023; accepted 6 October 2023; published 27 October 2023)

In this paper, we investigate the dynamics of a wind turbine wake for three different ground surface roughness lengths, i.e., $k_0 = 0.001, 0.01, 0.1$ m. The computational domain is very long [until $215D$ (D is the rotor diameter) wind turbine downwind], with the attempt to include the entire recovery process of a wind turbine wake. The streamwise variations of velocity deficit and turbulence intensity are analyzed. The focus of this paper is how flow structures of different scales vary as they pass through a wind turbine and travel to further downwind locations. Three different trends depending on scales are observed: (1) energy is added to motions of small scales ($<1D$) immediately in wind turbine's downwind, (2) energy for motions of scales in the range of $1D$ to $3.2D$ is first extracted by the wind turbine and then increased by the wake to a level higher than the inflow, and (3) energy for motions of scales greater than $3.4D$ is first extracted by the wind turbine, and then monotonically increase to the inflow level without a maximum. Finally, the energy density in scale space and its evolution in the streamwise direction are examined, showing the range of scales affected by a wind turbine and its wake.

DOI: [10.1103/PhysRevFluids.8.104605](https://doi.org/10.1103/PhysRevFluids.8.104605)

I. INTRODUCTION

Wakes act as the medium for the interference of wind turbines in a wind farm. As a wind turbine extracts kinetic energy from the wind, together with the loss of mean kinetic energy (MKE), the turbulence kinetic energy (TKE) in its wake is affected as well. Understanding the streamwise variation of turbulence in wake is of both fundamental and practical importance. It provides insights on how coherent wake structures interact with sheared turbulent flows, and the theoretical basis for developing engineering models for reducing the dynamic loads caused by wind turbine wakes. This paper aims to investigate the evolution of turbulence of various scales in a wind turbine wake, which is designed being long enough for the wake to achieve a fully recovered state.

It was shown in both numerical simulations and experiments that the TKE in a wind turbine wake's top-tip region first increases as the tip shear layer expands in the radial direction, interacting with the inner part of the wake and the ambient flow [1,2]. Then a peak of the maximum appears, with its strength and location depending on several factors, such as the inflow turbulence [3,4] and the blade design [5], etc. After the peak, the TKE decays at further turbine downwind locations [6]. The increase of TKE is associated with the breakdown of tip vortices and the onset of wake meandering. Lignarolo *et al.* showed that the pairing instability and the leapfrogging instability govern the breakdown of tip vortices [7]. Complex tip vortex structures with elongated tails and

*Corresponding author: xyang@imech.ac.cn

secondary vortices were observed in both field and large-eddy simulations (LESs), for which the centrifugal instability plays a role [8].

Most of the existing numerical and experimental studies on wake meandering have been focused on wind turbine downwind locations no further than $20D$ (where D is rotor diameter). For instance, the wake meandering of a 2.5 MW wind turbine was investigated until $5.1D$ in the work by Heisel *et al.* [9]. In the work by Medici and Alfredsson [10], the measurements were taken until $9D$ wind turbine downwind. Iungo *et al.* [11] carried out the analysis of wake meandering until $10D$ rotor downwind with a focus on the dynamics within $4.5D$ turbine downwind. Chamorro and Porté-Agel [12] investigated the effects of thermal stability on wake statistics with a focus the wake meandering at $5D$ rotor downwind. The wake dynamics of a hydrokinetic turbine were investigated experimentally by Chamorro *et al.* [13] until $9D$ rotor downwind with a focus on the wake meandering at $2D$ and $4D$ rotor downwind. The frequency characteristics of a rotor's wake for different tip speed ratios were investigated in a water flume by Okulov *et al.* [14] until approximately $5D$ rotor downstream. A review on wind tunnel experiments can be found in Ref. [15]. For numerical simulations, without the limitation of the experimental facility, a long computational domain can be employed. For instance, in the study conducted by Stevens *et al.* [16], the wake statics until $36D$ rotor downwind were examined, focusing on the comparisons of the actuator line and actuator disk (AD) predictions with measurements. Wu and Porté-Agel [17] evaluated the predictive capability of different rotor models until $20D$ wind turbine downwind. Xie and Archer [18] studied the mean and turbulent properties of the wake generated by a single wind turbine until $25D$ rotor downwind.

There exist two mechanisms for the onset of wake meandering [19]: (1) the inflow large-eddy mechanism, in which the turbine wake is considered as a passive scalar advected by the inflow large eddies and (2) the shear-layer instability mechanism, in which the onset of wake meandering is considered being similar to that of vortex shedding from bluff bodies. Evidence from field measurements and LESs indicate the coexistence of the two mechanisms [9,20]. The large-eddy mechanism was employed in the dynamic wake meandering model developed at Denmark Technical University [21], with the Taylor Frozen flow hypothesis for describing the space-time evolution of inflow large eddies [22]. In the work by Yang [23], a neural network model was proposed to predict the instantaneous transverse wake positions using the streamwise and transverse velocities at two locations upstream of the wind turbine and its thrust and torque coefficients as the inputs, showing an important role of the latter for the model's prediction accuracy.

To establish a unified framework for modeling wake meandering, the range of validity of the assumptions for the two mechanisms and the interactions between the two need to be well understood. For the first mechanism to work, the inflow eddy needs to be larger (e.g., two times) than the rotor diameter [19]. The scale of the wake meandering due to the shear instability mechanism, on the other hand, is comparable to the rotor diameter, and is influenced by upstream small-scale disturbances [19]. The development of wake meandering is strongly associated with the process of energy transfer among turbulent flow structures of different scales after the extraction of MKE and TKE of certain scales by the wind turbine.

There are various techniques available for the multiscale analysis of turbulence. Here, we present an overview of a few such methods and their applications. Premultiplied spectra is commonly used in wind turbine wake studies to examine the characteristics of wake meandering [24,25] and to understand how wind turbine acts on the inflow turbulence [26]. Direct filtering of the velocity fluctuation is another convenient tool for multiscale analysis. For instance, Watanabe *et al.* [27] employed a scale decomposition method based on a local volume average to evaluate the subgrid-scale energy budget [28] near the turbulent/nonturbulent interface. Dong *et al.* [29] investigated the interscale kinetic energy transfer with the use of the Gaussian filter for the energy cascade of shear-dominated scales. Motoori and Goto [30] applied the Gaussian filter to the DNS velocity field to understand the generation mechanism of a hierarchy of multiscale vortices. Cimarelli and De Angelis [31] examined the scale-by-scale budget of TKE in a filtered velocity field from channel flow using the generalized Kolmogorov equation. The energy spectrum in wave-number space has been commonly used to describe turbulence statistics at different scales. It can provide insights

into the energy cascade in homogeneous isotropic turbulence [32]. However, the wake turbulence is usually inhomogeneous. Several attempts have been made to propose a definition of energy density or scale energy in physical space for inhomogeneous turbulence. For example, Davidson [33] proposed an energy density defined as the gradient of the second-order structure function. Hamba [34] introduced the separation derivative of the two-point velocity correlation as energy density. Then he improved this definition by introducing a Gaussian filter [35]. A recent work by Hamba [36] proposed an expression for inhomogeneous turbulence based on the filtered velocities.

In this paper, a very long (to $215D$ turbine's downwind) wind turbine wake is simulated using LESs with an AD model. We define a wake as fully recovered when the turbulence in the atmospheric boundary layer reaches an equilibrium state. Specifically, with this very long computational domain, we hope to obtain a state in which the energy distribution in the scale space barely changes in the turbine's downwind direction. The very far wake investigated in this paper is not directly related to the optimization of turbine placement and control for maximizing wind farm performance. However, it is associated with wakes of wind farms [37–43], i.e., being an idealized condition without wake interactions, such that the obtained data can be employed for validating models of wind farm wakes. It should be noted that the Coriolis force is not considered in this paper to simplify the analysis of wake dynamics, which should be kept in mind when employing the results in other works. The impact of the Coriolis force on wake dynamics has been investigated in the literature, for instance, works reported in Refs. [44,45] and the references cited therein. Besides examining the conventional wake statistics (e.g., velocity deficit, turbulence intensity, and wake meandering frequency), the velocity fluctuations at different scales, which are obtained via spatial filtering, are systematically investigated to probe into how inflow turbulence at different scales is affected by the wind turbine and vary in its wake. The uniqueness of this paper has three aspects: (1) it systematically analyzes how a wind turbine represented by an AD affects different-scale inflow turbulence, (2) it finds the critical length scales for a wind turbine changing its impacts on the inflow turbulence, and (3) it demonstrates the downwind variations of wake-added turbulence of different scales for almost the entire wake recovery process. Moreover, to the best of the authors' knowledge, it is one of the longest wake simulations of a stand-alone wind turbine to date, which shows how the signatures of wake meandering vary over a wide range of turbine downwind distances and can be employed for validating engineering wake models for the very far wake.

The rest of the paper is organized as follows. In Sec. II, we introduce the numerical methods and the case setup. In Sec. III A, we present and analyze the time-averaged statistics, including the velocity deficit, turbulence intensity, Reynolds stress, and the budget equation for MKE. Then we analyze the velocity fluctuations at different scales obtained using the sphere-averaged filter in Sec. III B. Finally, we draw the conclusions in Sec. IV.

II. NUMERICAL METHODS AND SIMULATION SET-UP

A. Numerical method

We carry out the simulation using the LES module of the Virtual Flow Simulator (VFS-Wind) code [46,47], which has been successfully employed in different applications, e.g., wind energy [48,49], hydrokinetic energy [50], pollutant transport [51], blood flows [52,53], flows over underwater vehicles [54,55], and rough wall turbulence [56].

The governing equations are the spatially filtered incompressible Navier-Stokes equations as follows:

$$J \frac{\partial U^i}{\partial \xi^i} = 0, \quad (1)$$

$$\frac{1}{J} \frac{\partial U^i}{\partial t} = \frac{\xi_l^i}{J} \left(-\frac{\partial (U^j u_l)}{\partial \xi^j} + \frac{\mu}{\rho} \frac{\partial}{\partial \xi^j} \left(\frac{g^{jk}}{J} \frac{\partial u_l}{\partial \xi^k} \right) - \frac{1}{\rho} \frac{\partial}{\partial \xi^j} \left(\frac{\xi_l^j p}{J} \right) - \frac{1}{\rho} \frac{\partial \tau_{lj}}{\partial \xi^j} + f_l \right), \quad (2)$$

TABLE I. Summary of the cases simulated in this paper.

| Case | $k_0(m)$ | $D(m)$ | $z_{\text{hub}}(m)$ | $\Delta x/D$ | $\Delta y/D$ | $\Delta z_{\text{min}}/D$ | N_x | N_y | N_z |
|------|----------|--------|---------------------|--------------|--------------|---------------------------|-------|-------|-------|
| 1 | 0.001 | 100 | 100 | 1/5 | 1/10 | 1/50 | 1126 | 1488 | 152 |
| 2 | 0.01 | 100 | 100 | 1/5 | 1/10 | 1/50 | 1126 | 1488 | 152 |
| 3 | 0.1 | 100 | 100 | 1/5 | 1/10 | 1/50 | 1126 | 1488 | 152 |

where $\xi_l^i = \partial \xi^i / \partial x_l$ are the transformation metrics, J is the Jacobian of the geometric transformation, u_i is the i th component of the velocity vector in Cartesian coordinates, $U^i = (\xi_m^i / J) u_m$ is the contravariant volume flux, $g^{jk} = \xi_l^j \xi_l^k$ are the components of the contravariant metric tensor, μ is the dynamic viscosity, p is the pressure, ρ is the density, f_i are the body forces for modeling wind turbine aerodynamics, and the subgrid stress τ_{ij} . In this paper, the subgrid stress term τ_{ij} is modeled using the Smagorinsky model [57] with the model coefficient determined using the dynamic procedure of Germano *et al.* [58].

An AD model based on the one-dimensional momentum theory [59] is employed to calculate the forces on the AD. The AD is discretized using triangular surface meshes, which are independent of the background grid nodes. In the AD model, the thrust T is computed as

$$T = \frac{1}{2} \rho C_T \pi R^2 U_{in}^2. \quad (3)$$

In the above equation, R is the rotor radius and the thrust coefficient C_T is computed using the axial induction factor a via $C_T = 4a(1 - a)$. The incoming downwind velocity U_{in} is computed using the disk-averaged velocity U_d via $U_{in} = U_d / (1 - a)$. The downwind velocity on the AD meshes is interpolated from the background grid nodes using the smoothed four-point cosine discrete delta function [60]. In the employed AD model, the thrust is uniformly distributed on the AD. With the thrust on the AD, the effect of the rotor on the incoming wind is then taken into account by distributing the thrust on the background grid nodes via the same discrete delta function.

Compared with the actuator line and actuator surface (AS) models, the AD model is competitive in terms of computational cost, which is preferred for the long wake simulations carried out in this paper. However, the accuracy of the AD model is low in the near wake where the coherent tip and hub vortices are not captured, which should be beared in mind when readers are interested in the near-wake ($x < 3D$) results. Studies in the literature [5,61] have demonstrated the capability of the AD model in predicting far wake ($x > 3D$) dynamics. The AD model employed in this paper has been systematically validated against the AS results, showing that the AD model can accurately predict the velocity deficit and turbulence statistics for $x > 3D$. More details can be found in Ref. [46] for the flow solver and in Ref. [62] for the AD model, respectively.

B. Case setup

In this section, we present the setups of the simulated cases. The axial induction factor is 0.25, resulting in $C_T = 0.75$, which is common for utility-scale wind turbines. As shown in Fig. 1, the simulated domain is rectangular with a size of $L_x \times L_y \times L_z = 225D \times 148.7D \times 10D$, where x , y , and z denote the streamwise, spanwise, and vertical directions, respectively, and $D = 100$ m is the rotor diameter. With a hub height of $z_{\text{hub}} = 100$ m, ten turbines are arranged into one row, and placed with the spanwise spacings $14D$ at $x = 0$. The computational domain is discretized by a Cartesian grid with grid nodes of $N_x \times N_y \times N_z = 1126 \times 1488 \times 152$. Table I shows that the grid is uniform in x and y directions, and is also uniform near the ground ($z \in (0, 1.5D)$) with $\Delta z = D/50$ and gradually stretched to the top boundary. This grid resolution is sufficient to capture wind turbine wake and wind farm wake according to Yang *et al.* [62,63].

The boundary conditions are set up as follows. The turbulent inflows applied at the inlet ($x = -10D$) are generated by a precursory simulation, in which the turbulent flow is fully developed.

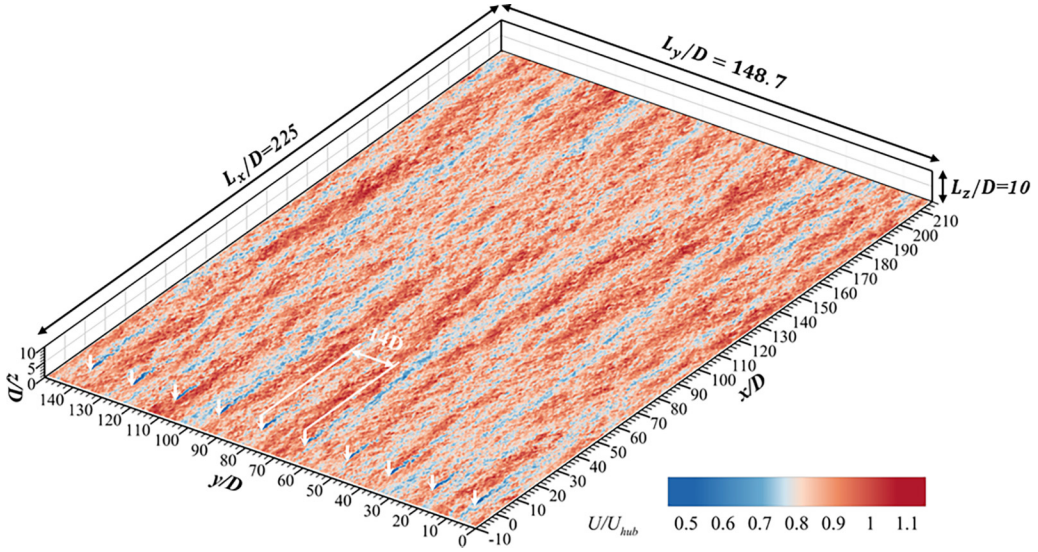


FIG. 1. Schematic of computational domain with the contours of the instantaneous streamwise velocity on the $x - y$ plane located at $z = z_{hub}$.

At the outlet ($x = 215D$), the Neumann boundary condition for velocity is applied. A wall model based on the logarithmic law for a rough wall is applied on the ground ($u/u_\tau = \frac{1}{\kappa} \ln(z/k_0)$, where u_τ is the friction velocity, $\kappa = 0.4$ is the Kármán constant, and k_0 is the roughness length). With the atmospheric condition set as neutral, the only variable for the simulated ABL is the roughness length of the ground surface. The employed roughness lengths, i.e., $k_0 = 0.001$ m, 0.01 m, and 0.1 m, are representative values for terrain class 2 smooth, 3 open, and 4 roughly open, respectively [64]. Figure 2 displays the main characteristics of the inflow over different ground surfaces. At the lateral and top boundaries, the free-slip boundary condition is applied. The simulation runs for 4000 time steps to fully develop the flow field. After that, the flow field is averaged for 26 000 steps to compute the flow statistics.

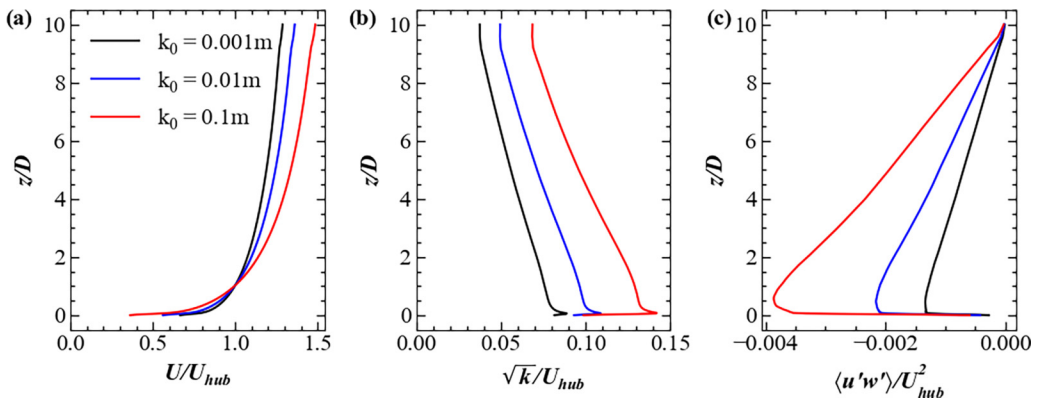


FIG. 2. Vertical profiles of (a) the time-averaged streamwise velocity, (b) turbulence intensity, and (c) the primary Reynolds shear stress of the incoming ABL flows over flat surfaces with the three different roughness lengths.

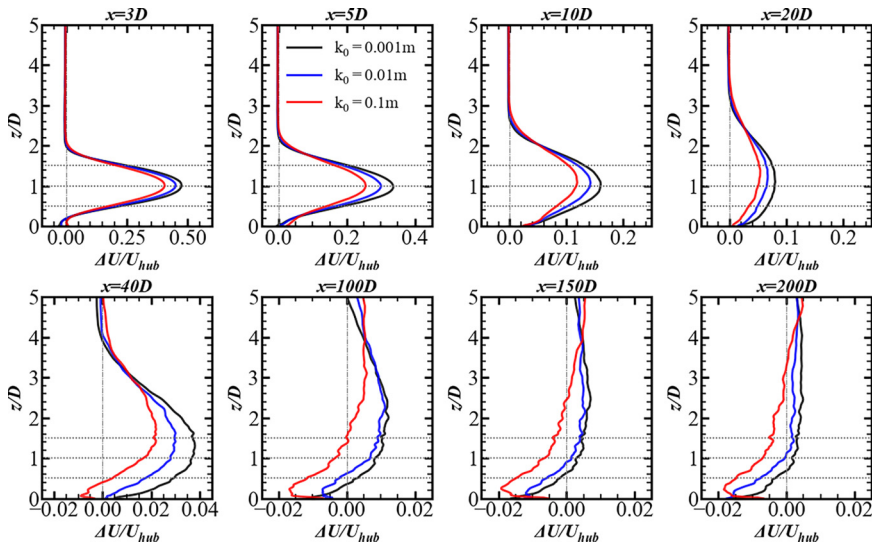


FIG. 3. Vertical profiles of mean streamwise velocity deficit at different wind turbine downwind locations. The horizontal dotted lines at $z/D = 1.5, 1,$ and 0.5 indicate the top tip, hub, and bottom tip positions, respectively. The vertical dot-dash line marks $\Delta U/U_{\text{hub}} = 0$.

III. RESULTS

A. Analysis of time-averaged flow field

In this section, we analyze the time-averaged flow fields from the simulated cases. For all the statistics of interest, we first compute them for each turbine by averaging over time, then average them across the ten turbines to obtain the plotted statistics.

1. Profiles of flow statistics

The vertical profiles of the mean streamwise velocity deficit for different ground surface roughness lengths are compared in Fig. 3 at different streamwise positions. As expected, the higher the inflow turbulence intensity, the faster the recovery of the wake velocity. With the mixing of the wake with the ambient flow, the velocity deficit region vertically expands as one travels in the downwind direction. At $x = 40D$, the maximum velocity deficit is less than 5% of U_{hub} for all three cases. At further wind turbine downwind locations, the velocity deficit in the near-wall region becomes negative, with a magnitude less than 2% of U_{hub} for all three cases and a higher magnitude for the case with higher roughness length. This phenomenon was also observed by Bodini *et al.* [65], for which the cause will be analyzed using the MKE budget equation.

In Fig. 4, the vertical profiles of turbulence intensity \sqrt{k} at different streamwise locations are plotted. At $x = 3D$, two peaks near the top and bottom tips are observed, which correspond to the shear layers at the corresponding locations. At $x > 5D$ and further turbine downwind locations, only the top peak persists with its vertical position moving upward as a result of wake expansion in the vertical direction. It is seen that the differences between the \sqrt{k} in the wake and the inflow are still significant at $x/D = 40$ (approximately 4% to 11% of the maximum of \sqrt{k}), and become extremely small at $x/D = 100$ (less than 3% of the maximum of \sqrt{k}) and further downwind locations. The streamwise variations of turbulence intensity is shown in Fig. 5. It is seen that the turbulence intensity of all cases rapidly increases in the near wake, reaches a peak, and gradually decays to that of the inflow. For the cases with larger k_0 , the location of the maximum \sqrt{k} is found being closer

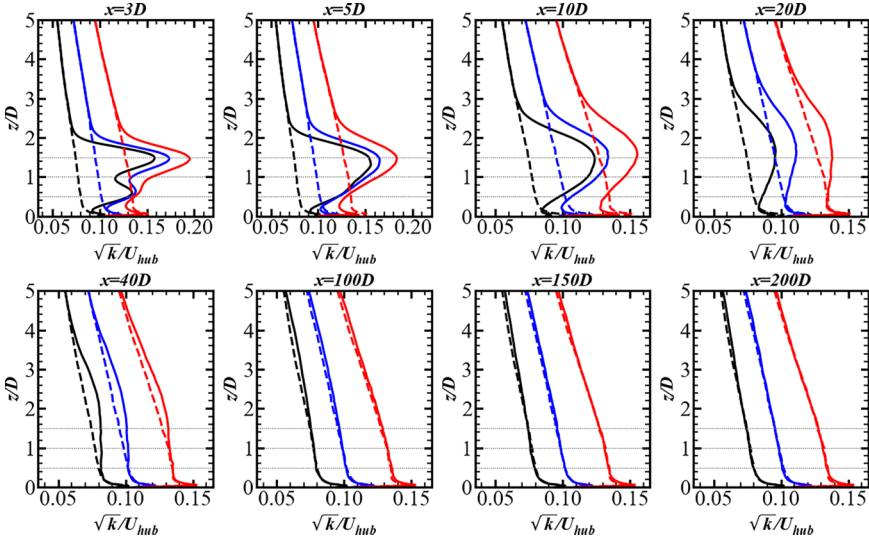


FIG. 4. Vertical profiles of turbulence intensity at different wind turbine downwind locations. The dashed lines represent the inflow turbulence intensity. The horizontal dotted lines at $z/D = 1.5, 1$ and 0.5 indicate the top tip, hub, and bottom tip positions, respectively.

to wind turbine, and recovers to that of the inflow at a higher rate (The location for $I/I_0 = 1.01$ is found at $77.2D, 60.4D,$ and $36.0D$ for the cases with $k_0 = 0.001, 0.01,$ and 0.1 m, respectively.).

Figure 6 shows the vertical profiles of the primary Reynolds shear stress $\langle u'w' \rangle$ at different turbine downwind locations, which measures the turbulent mixing of wake with ambient flow. At $x/D = 3$ and 5 , the vertical distribution is featured by two peaks, a negative one and a positive one located close to the top and bottom tips, respectively. At $x/D = 10$ and further turbine downwind locations, the turbulent mixing in the region above the wake dominates, with its magnitude larger than that of the inflow even at $x/D = 100$.

From the aspect of wind turbine placement and control, the impact of the very far wake (greater than $20D$ turbine downwind) is not a big concern, as the distance is significantly larger than the downwind turbine spacings often employed in the literature. The results presented above showed that the velocity deficit and wake-added turbulence can be significant at turbine downwind locations greater than $20D$, for which the maximal influenced distance varying with inflows.

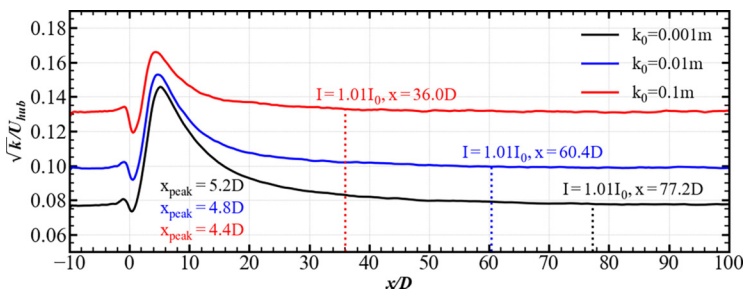


FIG. 5. Streamwise variations of turbulence intensity along the wake centerline for different ground surface roughness lengths. The vertical dotted lines indicate $I/I_0 = 1.01$ for 99% recovery of turbulence intensity.

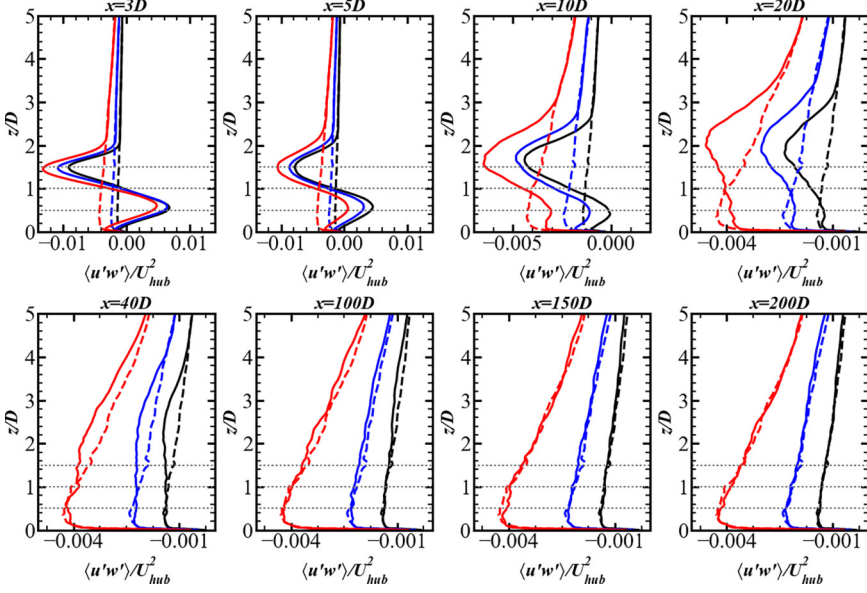


FIG. 6. Vertical profiles of primary Reynolds shear stress at different wind turbine downwind locations. The dashed lines represent the inflow Reynolds shear stress. The horizontal dotted lines at $z/D = 1.5$, 1 and 0.5 indicate the top tip, hub, and bottom tip positions, respectively. The legend is the same as Fig. 3.

2. Budget equation for mean kinetic energy

To probe into the mechanism for the recovery of the mean streamwise velocity, different terms in the budget equation for MKE are examined, which can be written as follows:

$$\begin{aligned} \frac{\partial \langle E \rangle}{\partial t} = & -\langle U_k \rangle \frac{\partial \langle E \rangle}{\partial x_k} - \frac{\partial}{\partial x_k} \left[\frac{\langle U_i \rangle \langle P \rangle}{\rho} \delta_{ik} + \langle u_i u_k \rangle \langle U_i \rangle - (v + v_t) \frac{\partial \langle E \rangle}{\partial x_k} \right] \\ & + \langle u_i u_k \rangle \frac{\partial \langle U_i \rangle}{\partial x_k} - (v + v_t) \frac{\partial \langle U_i \rangle}{\partial x_k} \frac{\partial \langle U_i \rangle}{\partial x_k}. \end{aligned} \quad (4)$$

For the present statistically steady problem, the time-derivative term is eliminated. The terms on the right-hand-side are the mean convection (MC), pressure transport (PT), turbulence convection (TC), viscous diffusion, turbulence production, and viscous dissipation terms, respectively.

Figure 7 shows the vertical variations of different terms in the MKE budget equation for the case with $k_0 = 0.001$ m. As seen, the MC term is mainly balanced by the TC term except for near-wall locations. At $x/D = 3, 5$ turbine downwind locations, the vertical distribution can be divided into three regions accordingly, i.e., the upper region located around the top boundary of the velocity wake (Fig. 3) with a positive MC term and negative TC term, the middle region located in the wake with a negative MC term and positive TC term, and the bottom region located around the bottom boundary of the velocity wake with a positive MC term and negative TC term. At $x/D = 10$ and further wind turbine downwind locations, the negative TC term in the bottom region is replaced by the positive one, associated with the end of wake expansion towards the wall. It is seen that at far wake locations ($x/D = 40$ and further), the positive TC term in the near-wall region is balanced by the PT term. Such a pressure transport term, however, is different from that due to the recovery of pressure in the near wake, which is observed at $3D$ and $5D$ turbine downwind (Fig. 7).

The TC term around the wake boundary, which plays a key role on the mixing between the high-momentum ambient fluid and the wake with velocity deficit, essentially extracts (negative) the momentum from the ambient fluid and disperse (positive) it in the wake. As shown in Fig. 8 for

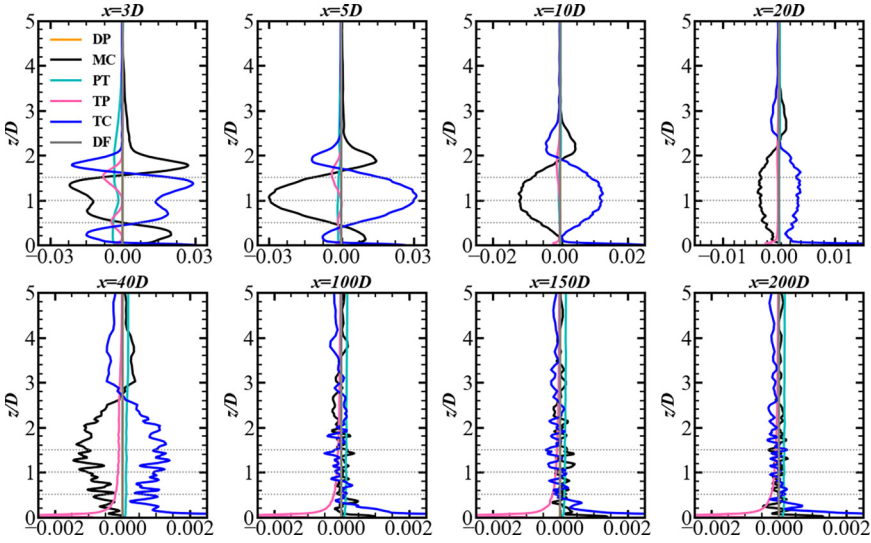


FIG. 7. Vertical profiles of the terms in the budget equation of mean kinetic energy for the case with $k_0 = 0.001$. The horizontal dotted lines at $z/D = 1.5, 1$ and 0.5 indicate the top tip, hub, and bottom tip positions, respectively.

different components of the TC term, the vertical component dominates the momentum mixing in the upper region at different turbine downwind locations. In the middle region, both the spanwise and vertical components are crucial for momentum mixing at $x/D = 3, 5, 10$. Starting from $x/D = 20$, the spanwise component becomes less important when compared with the vertical one. It is noted that at $x/D = 100, 150, 200$ turbine downwind locations the vertical component of the TC term (although the magnitude is small) is still negative in the upper region, which extracts

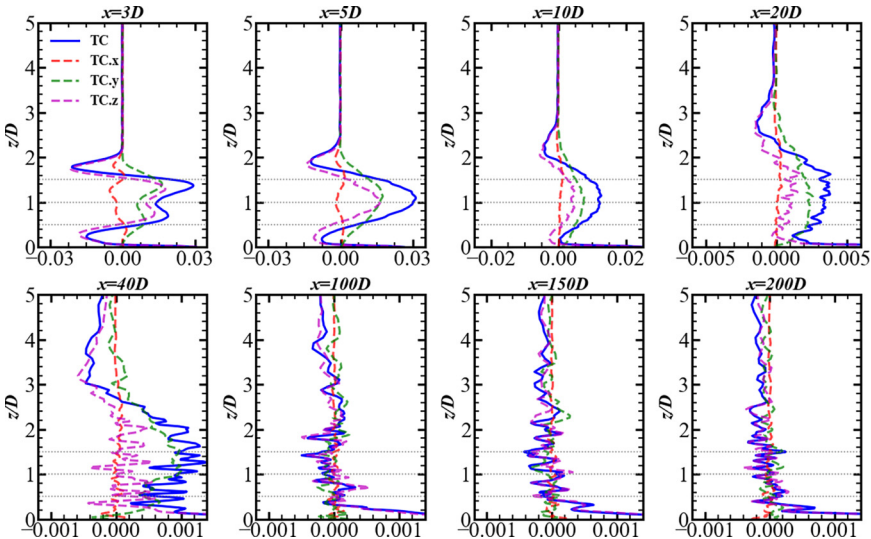


FIG. 8. Vertical profiles of the three components of the TC term in the MKE budget equation for the case with $k_0 = 0.001$. The horizontal dotted lines at $z/D = 1.5, 1$ and 0.5 indicate the top tip, hub, and bottom tip positions, respectively.

the local MKE, while it is positive (of high magnitude) in the near-wall region of narrow width, which enriches the local MKE, explaining the over-recovery of velocity (the negative velocity deficit shown in Fig. 3) in the near-wall region. In other words, it implies that the boundary layer does not yet achieve an equilibrium state at $40D$ and further turbine downwind locations, with the downward transport mechanism of momentum persisting at those locations. This nonequilibrium state is due to the large vertical range (which increases with turbine downwind distance) involved in the vertical momentum mixing, that the momentum extraction occurs around the top wake boundary, while the momentum enrichment happens in the near-wall region where the magnitude of the Reynolds stress term is large. One factor, that may introduce uncertainty to the results, is the relatively coarse grid employed in the simulation in which the viscous inner layer is not directly resolved.

B. Analysis of wake turbulence at different scales

As the wind turbine extracts the kinetic energy from the incoming wind, some turbulent flow structures lose their energy, meanwhile, the energy is accumulated at specific frequencies (such as those for wake meandering). In this section, we first show the amplitude of wake meandering at various turbine downwind locations in Sec. III B 1, then analyze how the energy of turbulent flow structures at different scales varies as the wind passing the wind turbine and at different turbine downwind locations by examining the premultiplied power spectral density (PSD) in Sec. III B 2 and the energy density in scale space in Sec. III B 3. To compute the energy density in scale space, an approach for the decomposition of energy density in scale space based on the sphere-averaged filter is derived and presented in Appendix B.

1. Amplitude of wake meandering

The amplitudes of wake meandering are examined for the three ground roughness lengths in this section. The frequency of wake meandering, which can be determined using the pre-multiplied PSD of the temporal series of velocity fluctuations, will be examined in Sec. III B 2.

The amplitude of wake meandering is computed using the instantaneous wake centers in the spanwise directions. Different methods for identifying instantaneous wake centers have been employed in the literature [66]. In this paper, the Gaussian fitting method [48,67,68] is employed. To eliminate undesired high-frequency fluctuations, which may cause problems during Gaussian fitting, the fifth-order Butterworth low-pass filtering technique is applied to the spanwise profiles of the instantaneous streamwise velocity deficit using the `butter` and `filtfilt` functions [69] from the `scipy.signal` module in Python. Due to the three-dimensional nature of wake meandering, it is possible that a wake may not exist on the horizontal plane, especially at far wake locations where the velocity deficit is small and the wake meandering amplitude is high. To avoid the error caused by the above issue, a validation step is conducted to determine the validity of the identified wake center. Specifically, the identified wake center y_c is considered valid only if wake center is surrounded by a velocity-deficit region, i.e., $y \in (y_c - 0.2D, y_c + 0.2D)$. The probability of having a wake on the horizontal plane (i.e., P_w) is defined using the number of valid wake centers identified during the considered temporal instants.

Figure 9 shows the standard deviation of instantaneous wake center positions σ_{y_c} , which represents the wake meandering amplitude. As seen, σ_{y_c} in all cases progressively increases along the flow direction until it reaches a stable value. For cases with larger k_0 , the values of σ_{y_c} are higher and reach a stable value at a relatively higher rate. The probability of locating a wake on the horizontal plane gradually decreases in the far wake region as expected.

2. Premultiplied power spectral density

The premultiplied PSD of the velocity fluctuations filtered using different scales are analyzed. The filtering of the velocity fluctuation is carried out using a sphere-averaged filter function, which

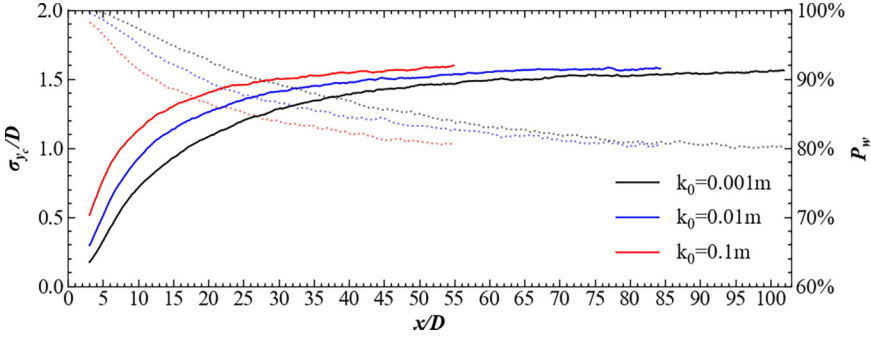


FIG. 9. Standard deviation of wake center position σ_{y_c} in the y - z plane at various streamwise locations for cases with different roughness lengths. The dashed lines indicate the probability of wake meandering occurring.

is defined as follows:

$$\bar{f}(r_d, s) = \frac{\epsilon(\frac{s}{2} - r_d)}{C_d s^d}, \quad r_d = \sqrt{\sum_{i=1}^d (x_i - x'_i)^2}, \quad (5)$$

where C_d is a normalization factor, s is the filter scale, d is the dimension of the filter, $\epsilon(x)$ is a step function. In this paper, the sphere-averaged filtering is performed on the $x - y$ plane located at hub height z_{hub} . With the sphere-averaged filter function, the velocity fluctuations with the scale larger than and smaller than the filter scale s are calculated as follows:

$$\bar{u}_i^{s^>}(x, y) = \bar{f} * u_i(x, y) = \int_{-\infty}^{+\infty} \int_{-\infty}^{+\infty} \bar{f}(x - x', y - y', s) u_i(x', y') dx' dy', \quad (6)$$

$$\bar{u}_i^{s^<}(x, y) = (1 - \bar{f}) * u_i(x, y) = u_i(x, y) - \bar{u}_i^{s^>}(x, y). \quad (7)$$

The characteristics of the premultiplied PSD of the grid-resolved streamwise velocity fluctuations are first examined in Fig. 10. As seen in Fig. 10(a), the energy at a range of frequencies is high in the wind turbine's wake from approximately $1D$ to $20D$ turbine downwind because of wake meandering and wake-added small scale turbulence. Instead of being a constant, it is observed that the meandering frequency varies in the wind turbine's downwind direction and recovers to that of the inflow at around $x = 20D$ according to Fig. 10(b). The Strouhal number of wake meandering shown in Fig. 10(b) is within the range of those reported in the literature. Some of them are given as follows: 0.23 (Okulov and Sørensen [70]), 0.28 (Chamorro *et al.* [13]), 0.15 (Foti *et al.* [24]), 0.33 and 0.402 (Chamorro *et al.* [12]), 0.25–0.3 (Foti *et al.* [25]), 0.26–0.47 (Heisel *et al.* [9]), and 0.15–0.25 (Medici and Alfredsson [71]). As for the magnitude of the peak of the premultiplied PSD normalized by the corresponding inflow turbulence intensity [Fig. 10(c)], it is higher for cases with lower inflow turbulence intensities (i.e., lower k_0), indicating a larger amplification factor for the range of wake meandering frequencies. Figure 11 shows the contours of premultiplied PSD of the velocity fluctuations ($\bar{u}_i^{s^<}$) with the scale less than the filter scale s in the $s^< - f$ plane. It is seen that the dominant frequency of the premultiplied PSD of $\bar{u}_i^{s^<}$ agrees with that of the wake meandering at $x/D = 5$, indicating the motions of the considered range of scales essentially ride on the coherent motion of wake meandering. With the increase of $s^<$ (from bottom to up), these figures tell the impact on the dominant frequency when including larger scales. For the inflow, the turbulent motions added by increasing the filter scale are observed on the left of the peak (with lower frequencies). At $x/D = 5$ turbine downwind, it was observed on both sides of the peak. The increase at the higher frequencies is due to wake meandering, which will be discussed in the following analyses. As expected, the magnitude of the premultiplied PSD increases when increasing the filter scale s . There is a critical filter scale s above which a significant increase in magnitude

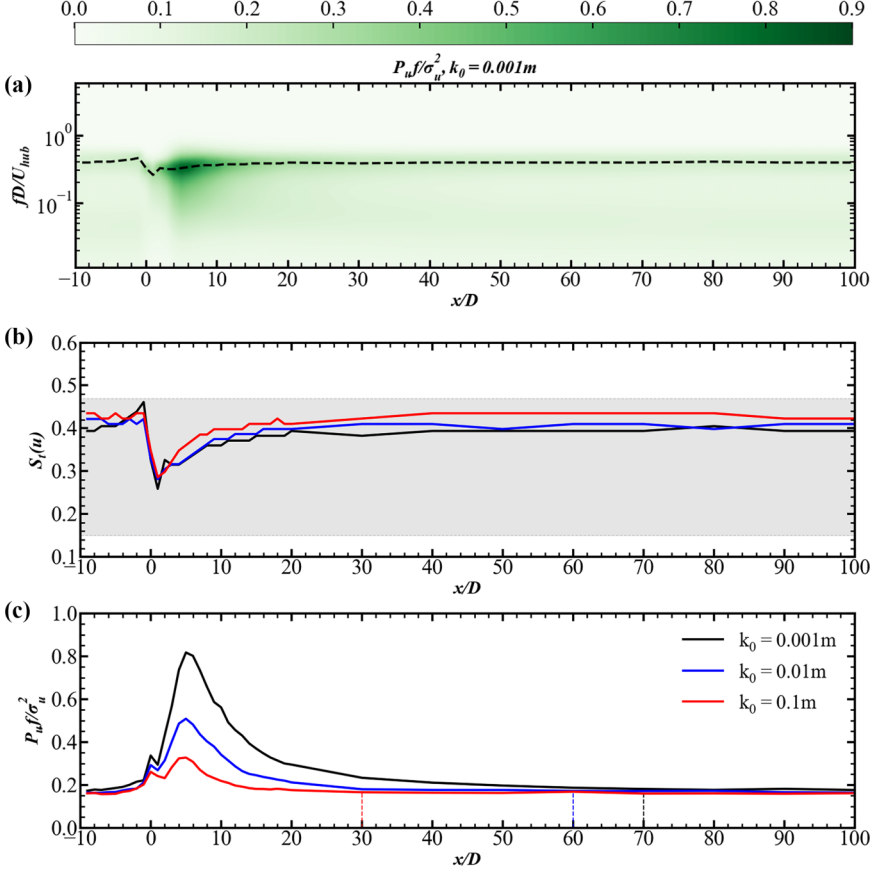


FIG. 10. (a) Contours of the premultiplied power spectral density (PSD) of the streamwise velocity fluctuations along the rotor centerline for the case with $k_0 = 0.001$ m, in which the black dashed line shows the peak of the premultiplied PSD at different streamwise locations. (b), (c) Frequency $S_r = fD/U_{\text{hub}}$ and magnitude of the peaks of the premultiplied PSD $P_u f / \sigma_u^2$ for cases with different roughness lengths, in which f is the frequency and σ_u^2 is the standard deviation of the inflow streamwise velocity fluctuations. The shaded region in (b) illustrates the range between the minimum and maximum values of the S_r of wake meandering reported in the literature. The vertical dotted lines in (c) represent the location where the amplitude of the premultiplied PSD recovers to 95% of the inflow.

occurs. Such critical filter scale, which is in the range of $0.8D$ to $1.2D$, is increased at $x/D = 5$ turbine downwind location. The critical filter scale essentially tells the length scales, which are most influenced by the wind turbine wake. It can be expected that such length scales are close to the rotor diameter, with the Strouhal number in the order of 1 as shown in Fig. 11. However, the corresponding energy-containing flow structures are yet to be explored, which may be a promising subject for future work.

After showing the premultiplied PSD of the velocity fluctuations ($\bar{u}_i^{s^c}$) at different streamwise locations, the streamwise variations of the maximum magnitude of the premultiplied PSD and the corresponding Strouhal number $S_r = f_{\text{peak}}D/U_{\text{hub}}$ of the peak frequency are shown in Figs. 12 and 13, respectively, for different filter scales s . It is seen in Fig. 12 that the maximum magnitude of the premultiplied PSD of $\bar{u}_i^{s^c}$ is larger and decreases at a slower rate in the turbine downwind direction for larger filter scale s .

Keeping in mind that increasing the filter scale acts as adding large scales to small scales, the streamwise extent of the region with the maximum magnitude of the premultiplied PSD higher than

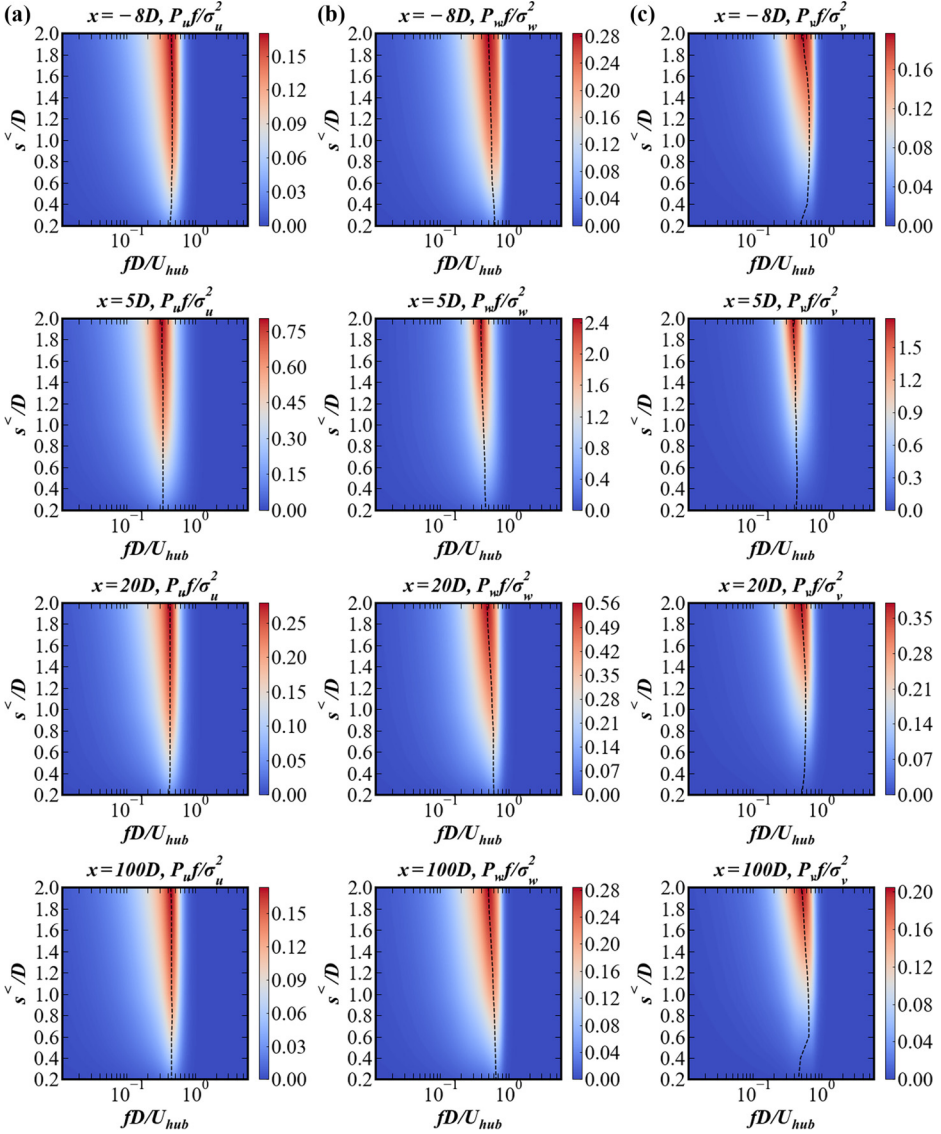


FIG. 11. Premultiplied PSD for (a) streamwise, (b) spanwise, and (c) vertical component of the velocity fluctuations ($\bar{u}_i^{s^<}$) with the scale smaller than the filter scale s in $s^< - f$ plane at different streamwise positions for the case with $k_0 = 0.001$ m. The dashed line shows the peak of the premultiplied PSD for different filter scales.

the inflow shows the influence range of the added large scales, which is approximately $20D$ to $30D$ for $s^< = 2D$. As for the frequency (the peak frequency shown in Fig. 13) corresponding to the maximum magnitude of the premultiplied PSD, it decreases in the wake of the wind turbine and recovers to that of the inflow at further turbine downwind locations. The recovery rate is similar for different filter scales, and is the lowest for the spanwise component and the highest for the vertical component, respectively. So far, the analysis of the premultiplied PSD has been focused on the velocity fluctuations ($\bar{u}_i^{s^<}$) with the scale smaller than the filter scale s . In Fig. 14, the premultiplied PSDs of the velocity fluctuations ($\bar{u}_i^{s^>}$) with a scale larger than s are examined. It is seen in Fig. 14(a) that two peaks exist in the premultiplied PSD of the streamwise velocity fluctuations $\bar{u}^{s^>}$ of the

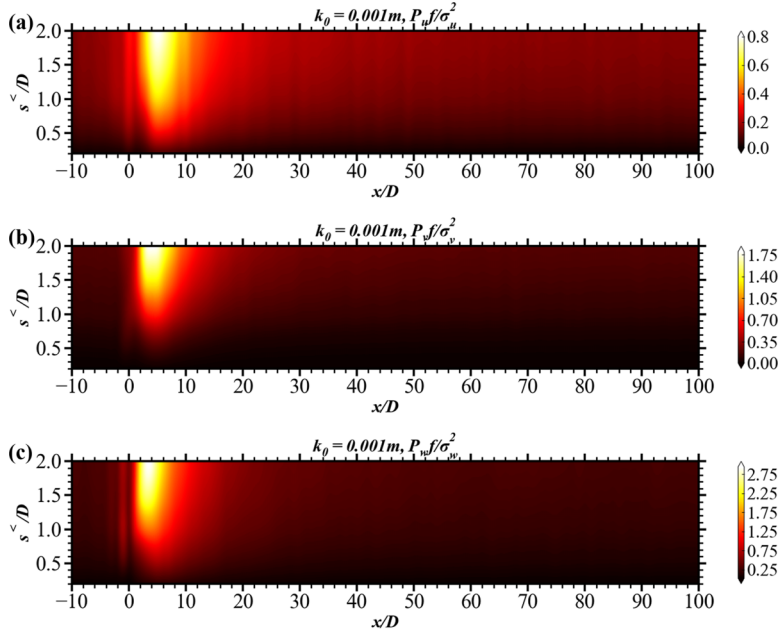


FIG. 12. Contours of the maximum magnitude of the pre-multiplied PSD for (a) streamwise, (b) spanwise, and (c) vertical component of the velocity fluctuations ($\bar{u}_i^{s^*}$) with the scale smaller than the filter scale s for the case with $k_0 = 0.001$ m.

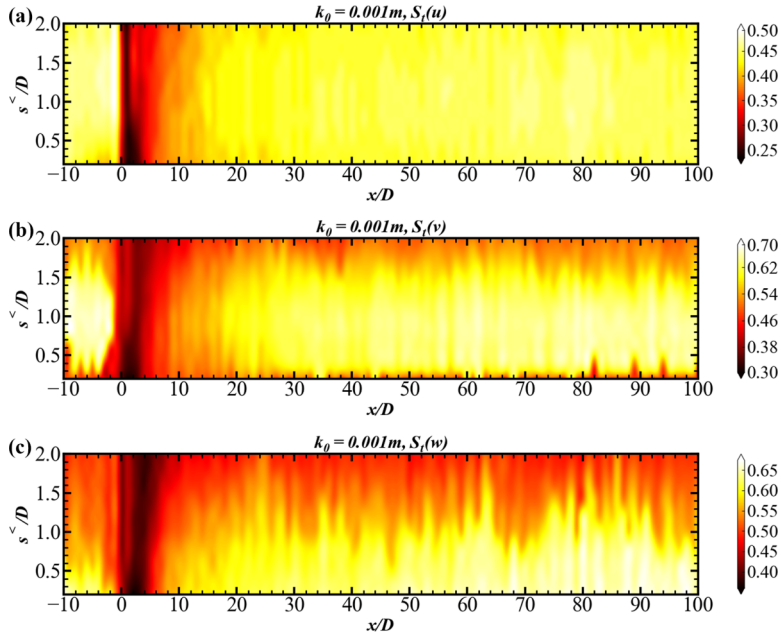


FIG. 13. Contours of the Strouhal number of the peak frequency $S_r = f_{\text{peak}} D / U_{\text{hub}}$ of the pre-multiplied PSD for (a) streamwise, (b) spanwise, and (c) vertical component of the velocity fluctuations ($\bar{u}_i^{s^*}$) with the scale smaller than the filter scale s for the case with $k_0 = 0.001$ m.

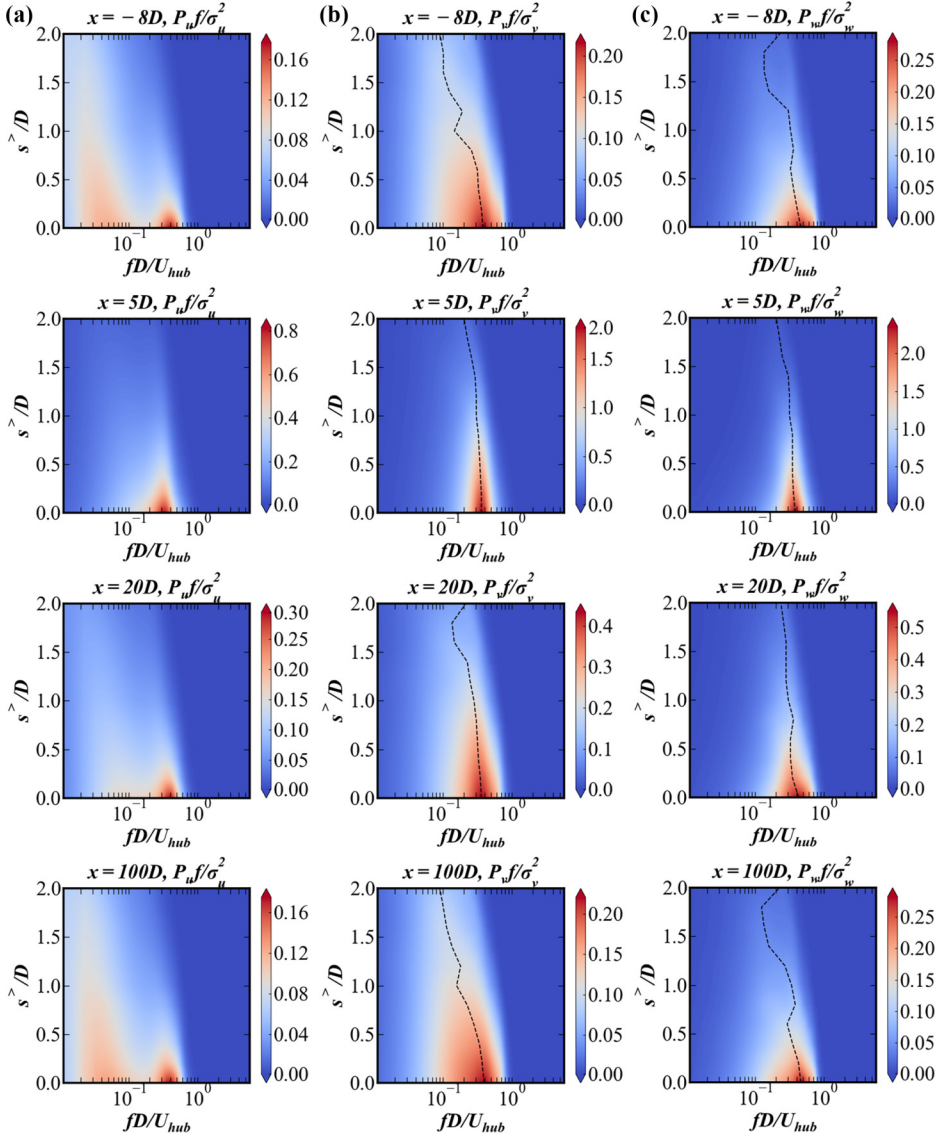


FIG. 14. Premultiplied PSD for (a) streamwise, (b) spanwise, and (c) vertical components of the velocity fluctuations ($\bar{u}_i^{s^>}$) with the scale larger than the filter scale s in $s^> - f$ plane at different streamwise positions for the case with $k_0 = 0.001$ m. The dashed line shows the peak of the premultiplied PSD in different filter scales.

inflow and the very far wake locations (e.g., $x/D = 100$), i.e., one at low frequencies and the other one at relatively high frequencies, with that the former ones persist and move to even lower values and the latter ones decay quickly when increasing the filter length scale s (i.e., removing the scales smaller than s). The low-frequency peak is from the inflow, for which the energy will be extracted by the wind turbine and gradually recovers to that of the inflow at further turbine downwind locations. At $x/D = 5$ turbine's downwind, the peak of low frequency disappears, while the magnitude of the high-frequency peak is increased with the corresponding frequency relocated to higher values close to the wake meandering frequency. It is also noted that the dominant frequencies at $x/D = 5$ are

skewed to lower frequencies when increasing s . At further wind turbine downwind locations, the peak of low frequency reappears with a weakened peak of high frequency.

For the other two components of the velocity fluctuations (i.e., $\bar{v}^{s^>}$ and $\bar{w}^{s^>}$), variations in the streamwise direction similar to that of $\bar{u}^{s^>}$ are observed except that only one peak exists. Overall, this figure shows the process of energy transfer from large scales of the inflow to the wake meandering scale in wind turbine wake and vice versa during the recovery of in the very far wake. The exact variations of different scales will be examined in the next section.

3. Energy density in scale space

The energy density in scale space is examined in this section, which is defined as follows:

$$E(\mathbf{x}, s) = -\frac{\partial \bar{Q}}{\partial s}, \quad (8)$$

where $\bar{Q} = \frac{1}{2} \langle \bar{u}_i^{s^>} \bar{u}_i^{s^>} \rangle$ is the TKE computed using the sphere-averaged filtered velocity fluctuations $\bar{u}_i^{s^>}$ [Eq. (6)]. The energy density $E(\mathbf{x}, s)$ in scale space should have the following two properties [33]:

$$k(\mathbf{x}) = \int_0^\infty E(\mathbf{x}, s) ds, \quad (9)$$

$$E(\mathbf{x}, s) \geq 0, \quad (10)$$

where $k(\mathbf{x}) = \frac{1}{2} \langle u_i u_i \rangle$ is TKE. To the best of our knowledge, a definition with both properties does not exist yet. Several definitions for energy density or scale energy have been proposed in the literature [34–36, 72, 73]. The definition employed in this paper follows that by Hamba [36], in which the filtered velocities were employed to obtain an expression for the scale-space energy density. The difference is that the filtered velocity in this paper is obtained using the sphere-averaged filter [Eq. (5)] instead of the Gaussian filter employed by Hamba [36]. With the assumption that the energy density at infinite large scale is zero, i.e., $E(\mathbf{x}, \infty) = 0$, the current definition [Eq. (8)] satisfies Eq. (9). It will also be shown that $E(\mathbf{x}, s)$ is non-negative in the horizontal plane located at turbine hub height. For detailed descriptions of energy density, including decomposition of energy density and energy density in homogeneous isotropic turbulence, please refer to Appendix B. Figure 15 shows the contours of energy density for cases with different roughness lengths. It is seen that the high energy density is distributed in a triangular shape region in the $x-s$ plane, with the peak located at around $x/D = 5$. In the immediate downwind of the wind turbine, the energy density varies in the streamwise direction in different ways for different scales. For the large scale, the energy density first decreases, and then increases to the peak at around $x/D = 5$. For the small scale, on the other hand, the energy density directly increases to the peak at around $x/D = 5$. As one travels to further turbine downwind locations, the energy density decays for all scales with a relatively higher rate for the large scales. To further examine how the energy of different scales varies in the streamwise direction, the energy density integrated over a range of scales, i.e., the TKE $k(s_1, s_2)$ of the motions with the scale between s_1 and s_2 , which is calculated via

$$k(s_1, s_2) = \int_{s_1}^{s_2} E(\mathbf{x}, s') ds' \quad (11)$$

is examined. Figure 16 shows $k(s_1, s_2)/k(x)$ as a function of streamwise locations, where the scale difference, $\Delta s/D = (s_2 - s_1)/D = 0.2$, is fixed, except when $s_1/D = 2$ (for which all the scales larger than $2D$ are integrated). Three different trends are observed. For motions with scales less than $1D$, the energy immediately increases in the wind turbine's wake, with the peak located around $5D$ turbine downwind, and then gradually decreases to the inflow level. For motions with scales in the range of $1D$ to $3.2D$, the energy first decreases in the very near wake ($<1D$), increases to a peak ($\sim 5D$) higher than the inflow, and decreases to the inflow level. For motions with scales greater than $3.4D$, the energy also decreases first but then monotonically increases to the inflow

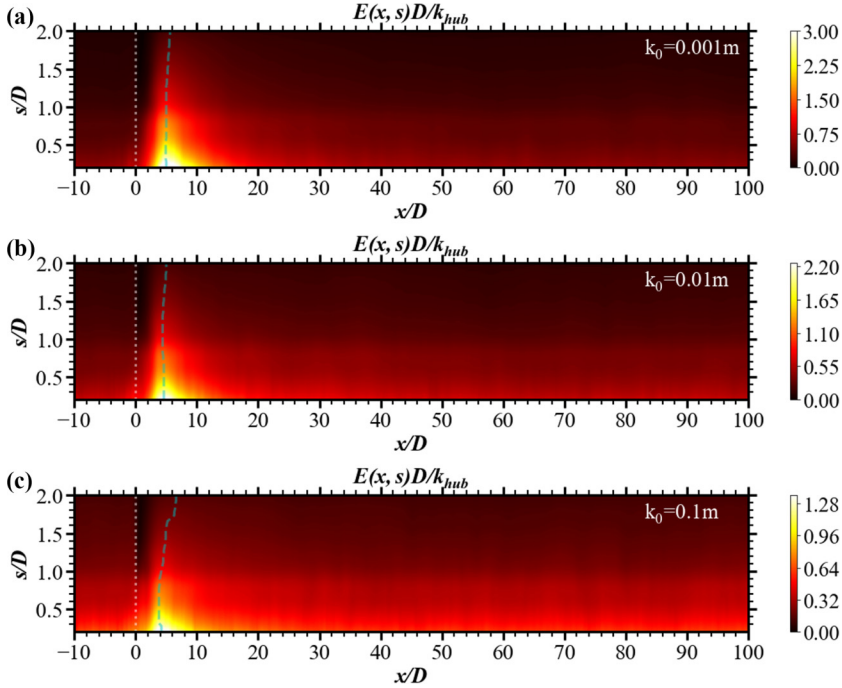


FIG. 15. Contours of energy density $E(x, s)$ [Eq. (8)] on the $x - s$ plane for (a) $k_0 = 0.001$ m, (b) $k_0 = 0.01$ m, and (c) $k_0 = 0.1$ m. The vertical white dotted line indicates the location of wind turbine. The green dashed line is the peak of energy density in the streamwise location for each scale s .

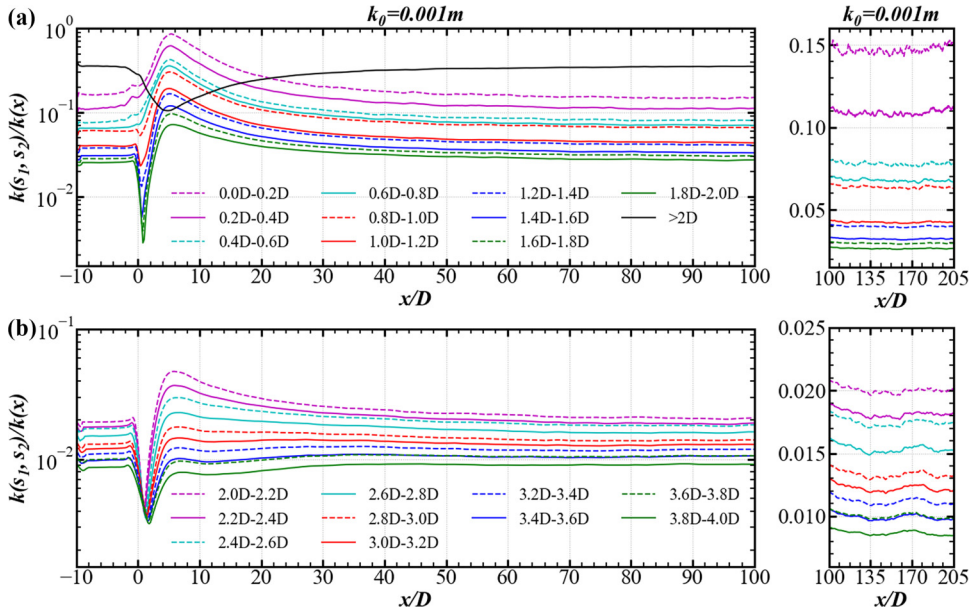


FIG. 16. Streamwise variations of the turbulence kinetic energy between two scales $k(s_1, s_2)$ nondimensionalized using the local turbulent kinetic energy $k(x)$ for the case with $k_0 = 0.001$ m.

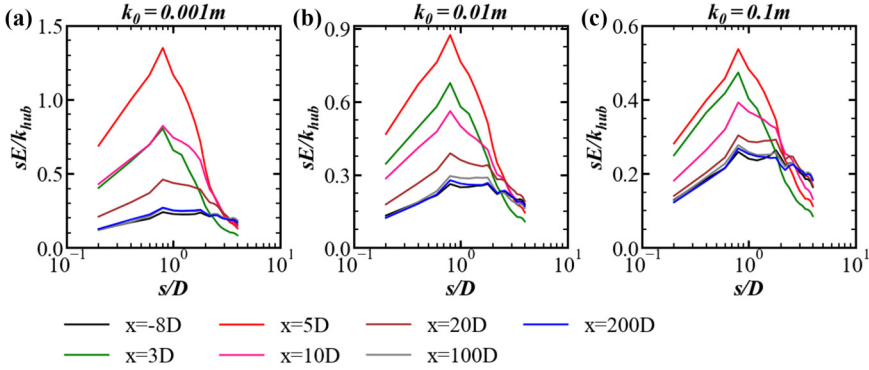


FIG. 17. Premultiplied energy density (sE) in scale space (s) at different streamwise locations for cases with different roughness lengths: (a) $k_0 = 0.001$ m, (b) $k_0 = 0.01$ m, and (c) $k_0 = 0.1$ m.

level without a peak higher than the inflow. From $100D$ to $200D$ turbine downwind positions, it is seen that the TKE for small scales reaches a steady state, while the TKE for large scales [e.g., $2.0 - 2.2D$ to $3.0 - 3.2D$ scales shown in Fig. 16(b)] somewhat keeps decreasing until around $135D$ turbine downstream. Similar trends are observed for $1.0 - 1.2D$ to $1.8 - 2.0D$ scales, which are difficult to notice in Fig. 16(a) because of the relatively large range of the vertical axis. Figure 17 shows the premultiplied energy density at several streamwise locations. For the three inflows, it is seen that the high energy region is located in the range of $0.8 < s/D < 1.8$. At $1D$ turbine downwind, the energy becomes less for $s/D > 1$, while higher for $x/D < 1$ when compared with the inflow. Moving further downwind, more energy is contained in motions with scales less than $2D$ with a peak around $s/D = 0.8$. At scales around $3D$ and larger, the increase in energy is minor or less than that of the inflow. At very far wake locations (e.g., $x/D = 100, 200$), the distribution of the premultiplied energy density recovers to that of the inflow. This figure clearly shows the process of energy transfer from the mean flow and large scales to small scales. The range of scales with increased energy is solely determined by the rotor scale, while the magnitude of the increase is governed by the inflow that higher inflow turbulence intensity is associated with a lower magnitude of increase ratio. It is noted that the energy density of the small scales predicted by the AD model might be different from a wind turbine in the relatively near wake region (e.g., $5D$ turbine downwind) where the effects of tip and hub vortex structures may still exist.

After showing wake statistics in this and previous sections, the mechanism for the wake meandering of the simulated cases is discussed here. First, it should be remarked that the tip vortices and hub vortex are not captured by the AD model. One consequence is that the variations of statistics in the near-wake region ($x < 3D$) might not accurately describe the wake of a wind turbine. Our previous works [20,74] showed the coexistence of two wake meandering mechanisms, i.e., inflow large eddy mechanism and shear-layer instability mechanism. The other consequence caused by the limitation of the AD model is that it may affect the intensity of the wake meandering caused by the shear layer instability, as shown by Kang *et al.* [75]. Increasing inflow turbulence intensity in general increases the amplitude of the wake meandering caused by the inflow large-eddy mechanism. Considering the increase of wake meandering amplitude with ground roughness length (Fig. 9), we speculate that the wake meandering of the simulated cases is largely caused by the inflow large eddies. On the other hand, it should also be noted that the wind turbine and its wake also impact the inflow large eddies including its energy intensity and characteristic length and time scales. However, this does not exclude the contribution from the shear-layer instability. The relatively higher increase in the turbine-added turbulence intensity (Fig. 5) for lower inflow turbulence intensity is directly related with the wake meandering caused by shear-layer instability, as evidenced by our previous study [49].

IV. CONCLUSIONS

In this paper, the characteristics of a very long wind turbine wake were analyzed using the data from LESs. In the simulation, the wind turbine aerodynamics was parameterized using the AD model. Three different ground surface roughness lengths (i.e., $k_0 = 0.001, 0.01, 0.1$ m) were considered.

The simulation results were first analyzed by probing into the vertical distributions of streamwise velocity deficit and turbulence intensity at various wind turbine downwind locations. The analyses showed that the region with velocity deficit and increased turbulence intensity shifts upward at very far wind turbine wake locations. The turbulence intensity in the wake recovers to that of the inflow at a higher rate for the case with higher ground roughness. One interesting observation was the over-recovery of the streamwise velocity in the near-ground region, which is the result of the persisting TC (of small magnitude) at very far wake locations. The premultiplied PSD was also examined, showing that the wake meandering frequency varies via turbine downwind distance, and recovers to that of the inflow at approximately $20D$ wind turbine downwind location.

Multiscale analyses were then carried out via spatial filtering to further analyze the wake dynamics. The premultiplied PSDs for the velocity fluctuations with length scale less than the filter scale ($\bar{u}_i^{s<}$) and greater than the filter scale ($\bar{u}_i^{s>}$) were examined. The rotor diameter D was observed from the premultiplied PSDs for $\bar{u}_i^{s<}$ being the critical length scale, beyond which a significant change in the magnitude of premultiplied PSD is observed. The premultiplied PSDs for $\bar{u}_i^{s>}$, on the other hand, show the process of energy transfer between the inflow turbulent flow structures and wake meandering. Different trends for different scales are observed from the streamwise variations of the energy at different scales. For motions of small scales ($<1D$), the energy immediately increases in the wind turbine's wake with the peak approximately located at $x \approx 5D$; for motions of scales in the range of $1D$ to $3.2D$, the energy first decreases in the very near wake ($<1D$), and then increases to a peak ($x \approx 5D$) higher than the inflow; for motions of scales greater than $3.4D$, the energy decreases first and then monotonically increase to the inflow level without a peak higher than the inflow. Examination of the energy density in scale space further confirms the above observation, shows that the energy in scale space is approximately concentrated in the range of $0.8D$ to $1.8D$, and demonstrates the energy transfer between the large and small scales at various turbine downwind locations.

The multiscale analyses in this paper were carried out by spatially filtering the velocity fluctuations, which do not differentiate whether they are from large coherent structures or small-scale fluctuations. Identifying the coherent motions and investigating how they interact with the incoherent fluctuations will be performed in our future study.

Moreover, although the present paper has been focused on the fluid dynamics aspect, the presented results are useful for the wind energy community. First, the obtained data can be employed for validating the engineering wake model in predicting the statistics of very far wake, which is required when assessing the wake effects on the downwind wind farms. Second, the scale around three rotor diameters ($3D$) is suggested to be the critical scale for inflow large eddies being able to advect the wake as passive scalars, which can be employed for developing dynamic wake models. This is based on the argument that the energy density of such large eddies will recover to that of the inflow without being intensified by the wake. Lastly, this paper suggests including the downwind variation of meandering frequency in the dynamic wake model.

ACKNOWLEDGMENTS

This paper was supported by the NSFC Basic Science Center Program for Multiscale Problems in Nonlinear Mechanics (No. 11988102), National Natural Science Foundation of China (No. 12172360), Institute of Mechanics, and Chinese Academy of Sciences.

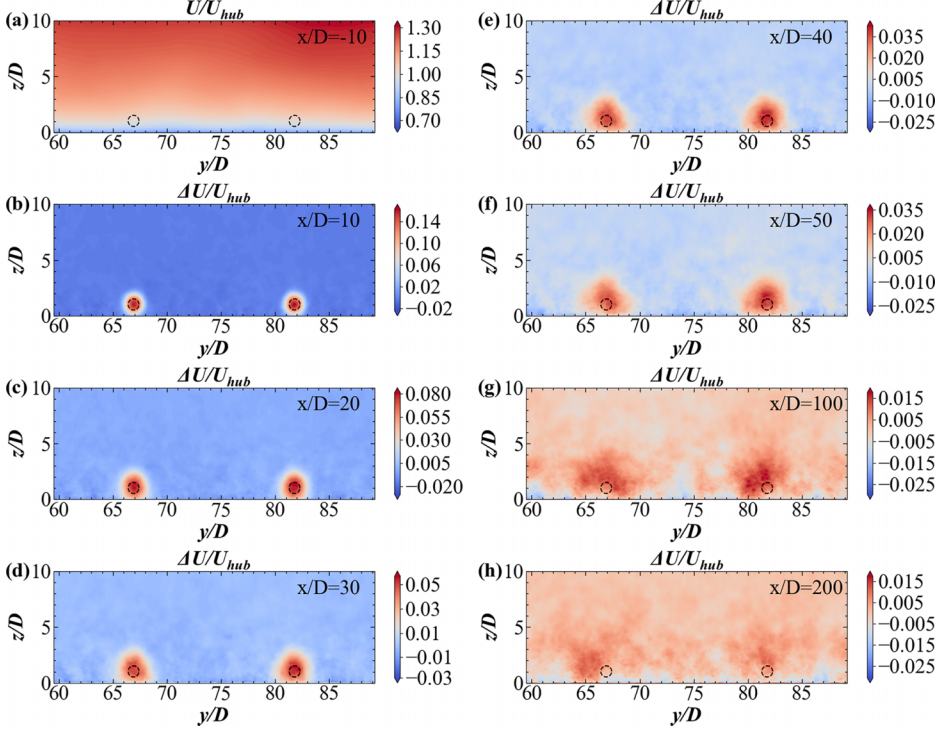


FIG. 18. Contour of (a) the mean streamwise velocity; (b)–(h) the mean streamwise velocity deficit in y - z plane at various streamwise locations for the case with $k_0 = 0.001\text{m}$. The dashed black lines indicate the disk of the wind turbine.

APPENDIX A: FLOW FIELD ON Y-Z PLANES

This Appendix shows the flow field on $y - z$ planes at different streamwise locations. It is to visually show the downwind footprints and the spanwise variations of wind turbine wakes, for which the latter ones are due to the spanwise variation of the inflow.

The mean streamwise velocity at the inlet (a) and velocity deficit (b)–(j) in the $y - z$ plane at various streamwise locations for cases with $k_0 = 0.001\text{ m}$ and $k_0 = 0.1\text{ m}$ are depicted in Figs. 18 and 19, respectively. It is evident that the wake feature illustrated by the velocity deficit persists at very far wake locations especially for the case with $k_0 = 0.001\text{ m}$. Figures 20 and 21 depict the TKE of the inflow (a) and wake-added TKE (b)–(j) in the $y - z$ plane at different streamwise positions for the cases with $k_0 = 0.001\text{ m}$ and $k_0 = 0.1\text{ m}$, respectively. It is seen that the wake-added turbulence is mainly located in the near-wall region for $z/D < 5$ and persists to very far wake locations, which is still around 10% of the inflow even at $100D$ turbine downwind for both inflow cases.

APPENDIX B: ENERGY DENSITY IN SCALE SPACE

In this Appendix, we derive a decomposition of energy density in scale space based on the sphere-averaged filter.

1. Three kinds of filtered velocity and energy

The first filtered velocity is written as

$$\bar{u}_l(\mathbf{x}, s) = \bar{f} * u_l = \int_{-\infty}^{+\infty} \bar{f}(r_d, s) u_l(\mathbf{x}') d\mathbf{x}', \quad (\text{B1})$$

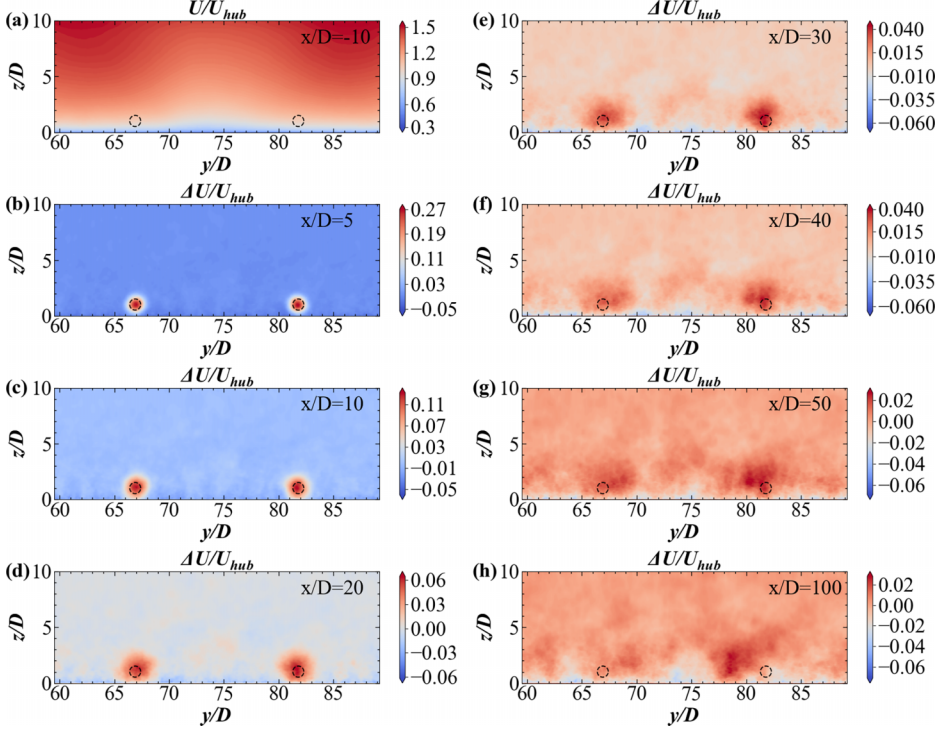


FIG. 19. Contour of (a) the mean streamwise velocity; (b)–(h) the mean streamwise velocity deficit in y - z plane at various streamwise locations for the case with $k_0 = 0.1m$. The dashed black lines indicate the disk of the wind turbine.

where \bar{f} is the sphere-averaged filter defined in Eq. (5) and d is the dimension of filter. Then the second filtered velocity can be written as

$$\hat{u}_l(\mathbf{x}, s) = -\frac{\partial \bar{u}_l}{\partial s} = \hat{f} * u_l = \int_{-\infty}^{+\infty} \hat{f}(r_d, s) u_l(\mathbf{x}') d\mathbf{x}', \quad (\text{B2})$$

$$\hat{f} = -\frac{\partial \bar{f}}{\partial s} = \frac{d}{s} \bar{f} - \frac{\delta(\frac{s}{2} - r_d)}{2C_d s^d}, \quad (\text{B3})$$

where $\delta(x)$ is a Dirac delta function. Assuming $\bar{u}_l(\mathbf{x}, \infty) = 0$, we have

$$\bar{u}_l(\mathbf{x}, s) = \int_s^\infty \hat{u}_l(\mathbf{x}, s') ds', \quad u_l(\mathbf{x}) = \int_0^\infty \hat{u}_l(\mathbf{x}, s') ds'. \quad (\text{B4})$$

As seen, the second filtered velocity indicates the distribution of the velocity in scale space. Then the third filtered velocity is defined as the first derivative of velocity in physics space, i.e.,

$$\tilde{u}_l^{(j)}(\mathbf{x}, s) = \frac{\partial \bar{u}_l}{\partial x_j} = \tilde{f}_j * u_l = \int_{-\infty}^{+\infty} \tilde{f}_j(r_d, s) u_l(\mathbf{x}') d\mathbf{x}', \quad (\text{B5})$$

$$\tilde{f}_j = \frac{\partial \bar{f}}{\partial x_j} = -\frac{x_j - x'_j}{r_d} \frac{\delta(\frac{s}{2} - r_d)}{C_d s^d}, \quad (\text{B6})$$

where the subscript $j \in [1, d]$ is a integer. With these filtered velocities, we can define three kinds of filtered energy as follows:

$$\text{the first filtered energy: } \bar{Q} = \frac{1}{2} \langle \bar{u}_i \bar{u}_i \rangle,$$

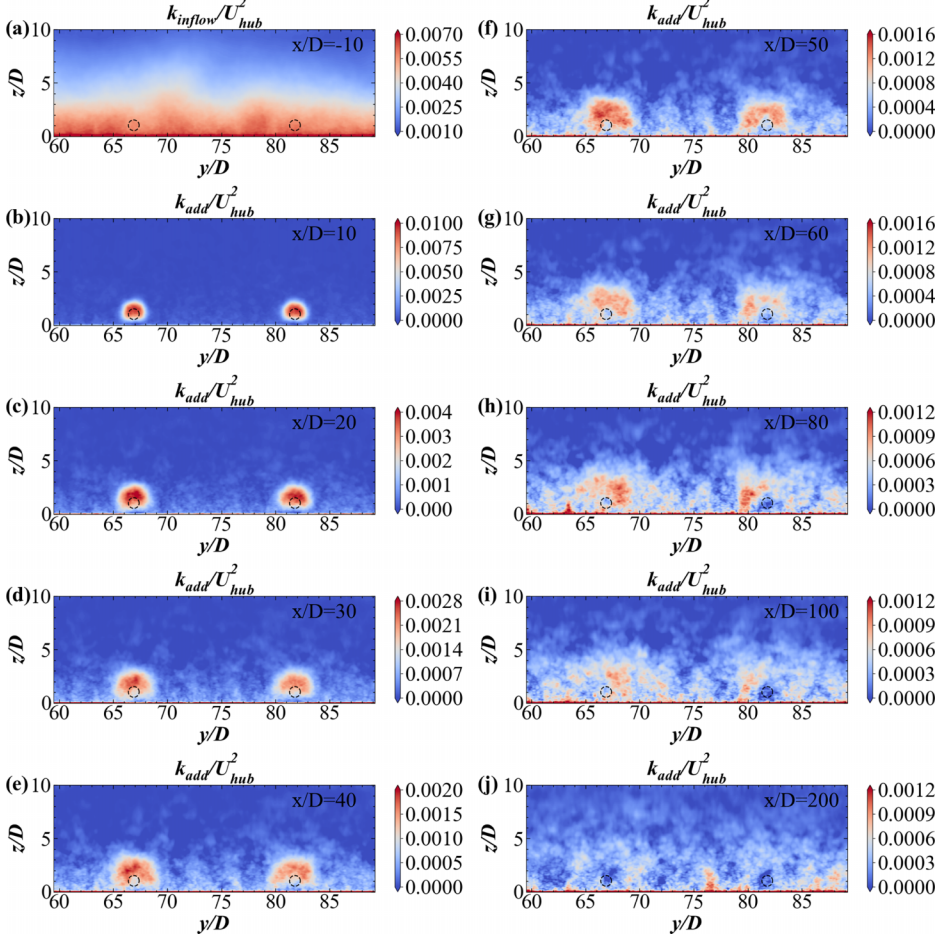


FIG. 20. Contour of (a) the turbulent kinetic energy from inflow; (b)–(j) the added turbulent kinetic energy $k_{add} = k - k_{inflow}$ in y - z plane at various streamwise locations for the case with $k_0 = 0.001m$. The dashed white lines indicate the disk of wind turbine.

$$\text{the second filtered energy: } \hat{Q} = \frac{1}{2} \langle \hat{u}_i \hat{u}_i \rangle,$$

$$\text{the third filtered energy: } \tilde{Q} = \frac{1}{2} \langle \tilde{u}_i^{(j)} \tilde{u}_i^{(j)} \rangle, \quad (\text{B7})$$

where $\langle \cdot \rangle$ indicates the time average and \tilde{Q} corresponds to the energy dissipation $\bar{\epsilon}$ in transport equation of the first filtered energy \bar{Q} . Then the energy density in scale space is defined as

$$E(\mathbf{x}, s) = -\frac{\partial}{\partial s} \bar{Q}(\mathbf{x}, s) = \langle \hat{u}_i \bar{u}_i \rangle. \quad (\text{B8})$$

In this way, the first filtered energy can be rewritten as

$$\bar{Q}(\mathbf{x}, s) = \int_s^\infty E(\mathbf{x}, s') ds', \quad k = \bar{Q}(\mathbf{x}, 0) = \int_0^\infty E(\mathbf{x}, s') ds', \quad (\text{B9})$$

where k is turbulent kinetic energy.

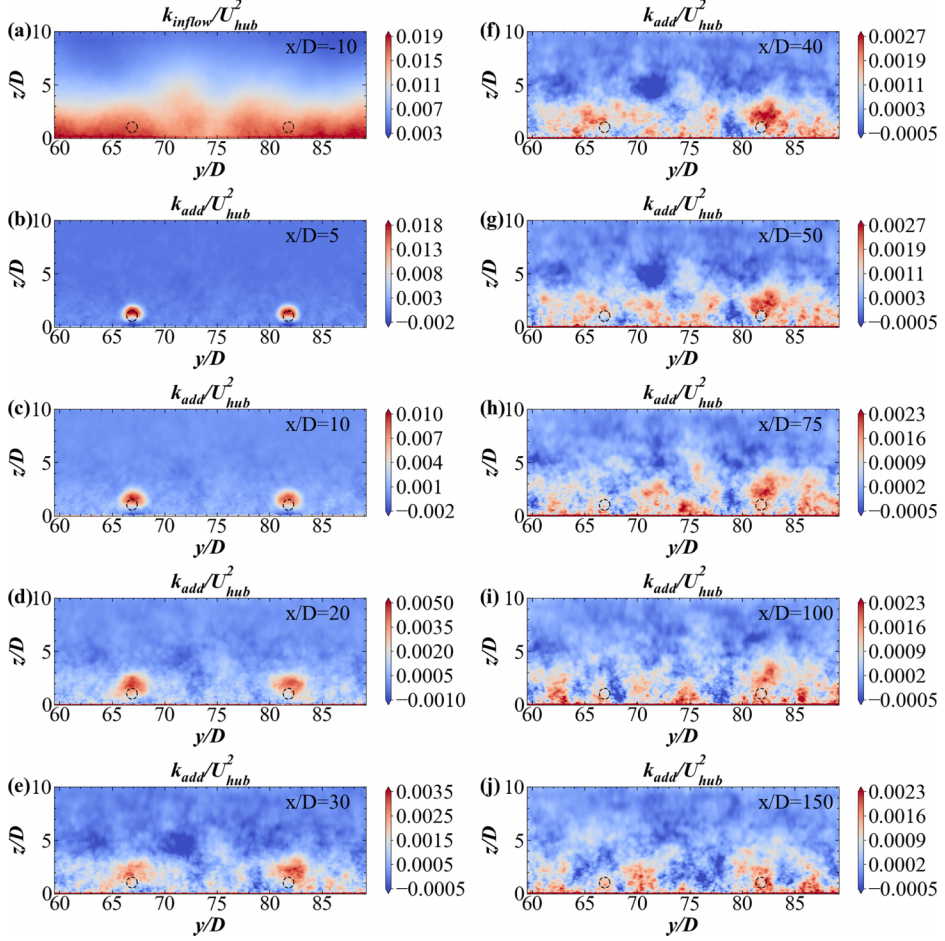


FIG. 21. Contour of (a) the turbulent kinetic energy from inflow; (b)–(j) the added turbulent kinetic energy $k_{\text{add}} = k - k_{\text{inflow}}$ in y - z plane at various streamwise locations for the case with $k_0 = 0.1\text{m}$. The dashed white lines indicate the disk of wind turbine.

2. Decomposition of energy density

According to the definition of the third filtered energy \tilde{Q} , we have

$$\tilde{Q} = \frac{1}{2} \langle \tilde{u}_i^{(j)} \tilde{u}_i^{(j)} \rangle = \frac{1}{2} \left\langle \frac{\partial \tilde{u}_i}{\partial x_j} \frac{\partial \tilde{u}_i}{\partial x_j} \right\rangle = \frac{1}{2} \left(\frac{\partial^2 \tilde{Q}}{\partial x_j \partial x_j} - \left\langle \tilde{u}_i \frac{\partial^2 \tilde{u}_i}{\partial x_j \partial x_j} \right\rangle \right), \quad (\text{B10})$$

$$\frac{\partial^2 \tilde{u}_i}{\partial x_j \partial x_j} = \frac{\partial \tilde{u}_i^{(j)}}{\partial x_j} = \frac{\partial \tilde{f}_j}{\partial x_j} * u_i, \quad (\text{B11})$$

where

$$\frac{\partial \tilde{f}_j}{\partial x_j} = \frac{\partial^2 \tilde{f}}{\partial x_j \partial x_j} = -\frac{1}{C_d s^d} \left(\frac{\partial}{\partial r_d} + \frac{d-1}{r_d} \right) \delta \left(\frac{s}{2} - r_d \right). \quad (\text{B12})$$

According to the derivative chain rule and the properties of Dirac delta function, Eq. (B12) can be rewritten as follows:

$$\frac{\partial \tilde{f}_j}{\partial x_j} = \frac{1}{C_d s^d} \left(2 \frac{\partial}{\partial s} - \frac{d-1}{s/2} \right) \delta \left(\frac{s}{2} - r_d \right). \quad (\text{B13})$$

Substitute the Dirac delta function which can be obtained from Eq. (B3) into Eq. (B13), we can easily obtain

$$\frac{\partial \tilde{f}_j}{\partial x_j} = -\frac{4}{s^{d+1}} \frac{\partial}{\partial s} (s^{d+1} \hat{f}). \quad (\text{B14})$$

So, we can rewrite Eq. (B11) and then substitute it into Eq. (B10), we can finally obtain

$$2\tilde{Q} = \frac{\partial^2 \tilde{Q}}{\partial x_j \partial x_j} + \frac{4}{s^{d+1}} \frac{\partial}{\partial s} (s^{d+1} E(\mathbf{x}, s)) + 8\hat{Q}. \quad (\text{B15})$$

Multiplying both sides of the equation above by s^{d+1} and integrating with respect to s , we obtain the decomposition of energy density as follows:

$$E(\mathbf{x}, s) = \frac{1}{s^{d+1}} \int_0^s s'^{d+1} \left[\frac{1}{2} \tilde{Q}(\mathbf{x}, s') - 2\hat{Q}(\mathbf{x}, s') - \frac{1}{4} \frac{\partial^2 \tilde{Q}(\mathbf{x}, s')}{\partial x_j \partial x_j} \right] ds'. \quad (\text{B16})$$

3. Energy density in homogeneous isotropic turbulence

In the case of the 3D sphere-averaged filter, the first filtered energy and the energy density are related to the Kolmogorov spectrum $E'(k)$ as follows:

$$\tilde{Q}(\mathbf{x}, s) = \int_0^\infty E'(k) e^{-sk} dk, \quad E(\mathbf{x}, s) = \int_0^\infty k E'(k) d^{-sk} dk. \quad (\text{B17})$$

In the inertial range, the Kolmogorov spectrum can be modeled as $E'(k) = K_0 \varepsilon^{2/3} k^{-5/3}$ [32]. When we substitute it into Eq. (B17), we obtain

$$E(\mathbf{x}, s) = K_0 \Gamma \left(\frac{1}{3} \right) \varepsilon^{2/3} s^{-1/3}, \quad (\text{B18})$$

where K_0 is the Kolmogorov constant, $\Gamma(x)$ is the gamma function, and ε is the energy dissipation rate.

-
- [1] R. J. A. M. Stevens and C. Meneveau, Flow structure and turbulence in wind farms, [Annu. Rev. Fluid Mech.](#) **49**, 311 (2017).
 - [2] F. Porté-Agel, M. Bastankhah, and S. Shamsoddin, Wind-turbine and wind-farm flows: A review, [Boundary-Layer Meteorol.](#) **174**, 1 (2020).
 - [3] M. Churchfield, S. Lee, J. Michalakes, and P. Moriarty, A numerical study of the effects of atmospheric and wake turbulence on wind turbine dynamics, [J. Turbul.](#) **13**, N14 (2012).
 - [4] X. Liu, Z. Li, X. Yang, D. Xu, S. Kang, and A. Khosronejad, Large-Eddy simulation of wakes of waked wind turbines, [Energies](#) **15**, 2899 (2022).
 - [5] G. Dong, Z. Li, J. Qin, and X. Yang, Predictive capability of actuator disk models for wakes of different wind turbine designs, [Renewable Energy](#) **188**, 269 (2022).
 - [6] Y. Zhang, Z. Li, X. Liu, F. Sotiropoulos, and X. Yang, Turbulence in waked wind turbine wakes: Similarity and empirical formulae, [Renewable Energy](#) **209**, 27 (2023).
 - [7] L. Lignarolo, D. Ragni, F. Scarano, C. S. Ferreira, and G. Van Bussel, Tip-vortex instability and turbulent mixing in wind-turbine wakes, [J. Fluid Mech.](#) **781**, 467 (2015).

- [8] X. Yang, J. Hong, M. Barone, and F. Sotiropoulos, Coherent dynamics in the rotor tip shear layer of utility-scale wind turbines, *J. Fluid Mech.* **804**, 90 (2016).
- [9] M. Heisel, J. Hong, and M. Guala, The spectral signature of wind turbine wake meandering: A wind tunnel and field-scale study, *Wind Energy* **21**, 715 (2018).
- [10] D. Medici and P.-H. Alfredsson, Measurements on a wind turbine wake: 3D effects and bluff body vortex shedding, *Wind Energy* **9**, 219 (2006).
- [11] G. V. Iungo, F. Viola, S. Camarri, F. Porté-Agel, and F. Gallaire, Linear stability analysis of wind turbine wakes performed on wind tunnel measurements, *J. Fluid Mech.* **737**, 499 (2013).
- [12] L. Chamorro and F. Porté-Agel, Effects of thermal stability and incoming boundary-layer flow characteristics on wind-turbine wakes: A wind-tunnel study, *Boundary-Layer Meteorol.* **136**, 515 (2010).
- [13] L. Chamorro, C. Hill, S. Morton, C. Ellis, R. E. A. Arndt, and F. Sotiropoulos, On the interaction between a turbulent open channel flow and an axial-flow turbine, *J. Fluid Mech.* **716**, 658 (2013).
- [14] V. L. Okulov, I. Naumov, R. F. Mikkelsen, I. K. Kabardin, and J. N. Sørensen, A regular Strouhal number for large-scale instability in the far wake of a rotor, *J. Fluid Mech.* **747**, 369 (2014).
- [15] R. He, H. Sun, X. Gao, and H. Yang, Wind tunnel tests for wind turbines: A state-of-the-art review, *Renewable Sustainable Energy Rev.* **166**, 112675 (2022).
- [16] R. J. A. M. Stevens, L. A. Martínez-Tossas, and C. Meneveau, Comparison of wind farm large eddy simulations using actuator disk and actuator line models with wind tunnel experiments, *Renewable Energy* **116**, 470 (2018).
- [17] Y.-T. Wu and F. Porté-Agel, Large-Eddy simulation of wind-turbine wakes: Evaluation of turbine parametrisations, *Boundary-Layer Meteorol.* **138**, 345 (2011).
- [18] S. Xie and C. Archer, Self-similarity and turbulence characteristics of wind turbine wakes via Large-Eddy simulation, *Wind Energy* **18**, 1815 (2015).
- [19] X. Yang and F. Sotiropoulos, A review on the meandering of wind turbine wakes, *Energies* **12**, 4725 (2019).
- [20] X. Yang and F. Sotiropoulos, Wake characteristics of a utility-scale wind turbine under coherent inflow structures and different operating conditions, *Phys. Rev. Fluids* **4**, 024604 (2019).
- [21] G. C. Larsen, H. A. Madsen, K. Thomsen, and T. J. Larsen, Wake meandering: A pragmatic approach, *Wind Energy* **11**, 377 (2008).
- [22] G. He, G. Jin, and Y. Yang, Space-time correlations and dynamic coupling in turbulent flows, *Annu. Rev. Fluid Mech.* **49**, 51 (2017).
- [23] X. Yang, Towards the development of a wake meandering model based on neural networks, in *Journal of Physics: Conference Series* (IOP Publishing, Bristol, UK, 2020), Vol. 1618, p. 062026.
- [24] D. Foti, X. Yang, M. Guala, and F. Sotiropoulos, Wake meandering statistics of a model wind turbine: Insights gained by large Eddy simulations, *Phys. Rev. Fluids* **1**, 044407 (2016).
- [25] D. Foti, X. Yang, and F. Sotiropoulos, Similarity of wake meandering for different wind turbine designs for different scales, *J. Fluid Mech.* **842**, 5 (2018).
- [26] L. Chamorro, M. Guala, R. E. A. Arndt, and F. Sotiropoulos, On the evolution of turbulent scales in the wake of a wind turbine model, *J. Turbul.* **13**, N27 (2012).
- [27] T. Watanabe, C. B. da Silva, and K. Nagata, Scale-by-scale kinetic energy budget near the turbulent/nonturbulent interface, *Phys. Rev. Fluids* **5**, 124610 (2020).
- [28] C. B. Da Silva and O. Métais, On the influence of coherent structures upon interscale interactions in turbulent plane jets, *J. Fluid Mech.* **473**, 103 (2002).
- [29] S. Dong, Y. Huang, X. Yuan, and A. Lozano-Durán, The coherent structure of the kinetic energy transfer in shear turbulence, *J. Fluid Mech.* **892**, A22 (2020).
- [30] Y. Motoori and S. Goto, Generation mechanism of a hierarchy of vortices in a turbulent boundary layer, *J. Fluid Mech.* **865**, 1085 (2019).
- [31] A. Cimarelli and E. L. De Angelis, Analysis of the Kolmogorov equation for filtered wall-turbulent flows, *J. Fluid Mech.* **676**, 376 (2011).
- [32] S. B. Pope, *Turbulent Flows* (Cambridge University Press, Cambridge, UK, 2000).
- [33] P. Davidson, *Turbulence: An Introduction for Scientists and Engineers* (Oxford University Press, Oxford, UK, 2015).

- [34] F. Hamba, Turbulent energy density and its transport equation in scale space, *Phys. Fluids* **27**, 085108 (2015).
- [35] F. Hamba, Turbulent energy density in scale space for inhomogeneous turbulence, *J. Fluid Mech.* **842**, 532 (2018).
- [36] F. Hamba, Scale-space energy density for inhomogeneous turbulence based on filtered velocities, *J. Fluid Mech.* **931**, A34 (2022).
- [37] M. B. Christiansen and C. B. Hasager, Wake effects of large offshore wind farms identified from satellite SAR, *Remote Sensing Environ.* **98**, 251 (2005).
- [38] C. B. Hasager, P. Vincent, J. Badger, M. Badger, A. Di Bella, A. Peña, R. Husson, and P. J. H. Volker, Using satellite SAR to characterize the wind flow around offshore wind farms, *Energies* **8**, 5413 (2015).
- [39] R. J. A. M. Stevens, Dependence of optimal wind turbine spacing on wind farm length, *Wind Energy* **19**, 651 (2016).
- [40] A. Platis, M. Hundhausen, M. Mauz, S. Siedersleben, A. Lampert, K. Bärfuss, B. Djath, J. Schulz-Stellenfleth, B. Canadillas, T. Neumann *et al.*, Evaluation of a simple analytical model for offshore wind farm wake recovery by in situ data and weather research and forecasting simulations, *Wind Energy* **24**, 212 (2021).
- [41] B. Cañadillas, M. Beckenbauer, J. J. Trujillo, M. Dörenkämper, R. Foreman, T. Neumann, and A. Lampert, Offshore wind farm cluster wakes as observed by long-range-scanning wind lidar measurements and mesoscale modeling, *Wind Energy Sci.* **7**, 1241 (2022).
- [42] A. H. Syed, J. Mann, A. Platis, and J. Bange, Turbulence structures and entrainment length scales in large offshore wind farms, *Wind Energy Sci.* **8**, 125 (2023).
- [43] Z. Wang, G. Dong, Z. Li, and X. Yang, Statistics of wind farm wakes for different layouts and ground roughness, *Boundary-Layer Meteorol.* **188**, 285 (2023).
- [44] M. Abkar and F. Porté-Agel, Influence of the coriolis force on the structure and evolution of wind turbine wakes, *Phys. Rev. Fluids* **1**, 063701 (2016).
- [45] M. F. Howland, A. Ghate, and S. Lele, Coriolis effects within and trailing a large finite wind farm, in *AIAA Scitech 2020 Forum* (Orlando, USA, 2020), p. 0994.
- [46] X. Yang, F. Sotiropoulos, R. J. Conzemius, J. N. Wachtler, and M. B. Strong, Large-Eddy simulation of turbulent flow past wind turbines/farms: The virtual wind simulator (VWiS), *Wind Energy* **18**, 2025 (2015).
- [47] X. Yang, D. Angelidis, A. Khosronejad, T. Le, S. Kang, A. Gilmanov, L. Ge, I. Borazjani, and A. Calderer, Virtual flow simulator, <https://doi.org/10.11578/dc.20171025.1758> (2015).
- [48] Z. Li and X. Yang, Large-Eddy simulation on the similarity between wakes of wind turbines with different yaw angles, *J. Fluid Mech.* **921**, A11 (2021).
- [49] Z. Li, G. Dong, and X. Yang, Onset of wake meandering for a floating offshore wind turbine under side-to-side motion, *J. Fluid Mech.* **934**, A29 (2022).
- [50] X. Yang, A. Khosronejad, and F. Sotiropoulos, Large-Eddy simulation of a hydrokinetic turbine mounted on an erodible bed, *Renewable Energy* **113**, 1419 (2017).
- [51] X. Yang and F. Sotiropoulos, On the dispersion of contaminants released far upwind of a cubical building for different turbulent inflows, *Build. Environ.* **154**, 324 (2019).
- [52] Y. Chen, X. Yang, A. J. Iskander, and P. Wang, On the flow characteristics in different carotid arteries, *Phys. Fluids* **32**, 101902 (2020).
- [53] X. He and X. Yang, Effects of exercise on flow characteristics in human carotids, *Phys. Fluids* **34**, 011909 (2022).
- [54] F. Liao, S. Wang, X. Yang, and G. He, A simulation-based actuator surface parameterization for Large-Eddy simulation of propeller wakes, *Ocean Eng.* **199**, 107023 (2020).
- [55] Z. Zhou, Z. Li, G. He, and X. Yang, Towards multi-fidelity simulation of flows around an underwater vehicle with appendages and propeller, *Theor. Appl. Mech. Lett.* **12**, 100318 (2022).
- [56] S. Li, X. Yang, and Y. Lv, Predictive capability of the logarithmic law for roughness-modeled Large-Eddy simulation of turbulent channel flows with rough walls, *Phys. Fluids* **34**, 085112 (2022).
- [57] J. Smagorinsky, General circulation experiments with the primitive equations: I. The basic experiment, *Mon. Weather Rev.* **91**, 99 (1963).

- [58] M. Germano, U. Piomelli, P. Moin, and W. H. Cabot, A dynamic subgrid-scale Eddy viscosity model, *Phys. Fluids* **3**, 1760 (1991).
- [59] M. Hansen, *Aerodynamics of Wind Turbines* (Earthscan, Routledge, London, UK, 2015).
- [60] X. Yang, X. Zhang, Z. Li, and G.-W. He, A smoothing technique for discrete delta functions with application to immersed boundary method in moving boundary simulations, *J. Comput. Phys.* **228**, 7821 (2009).
- [61] Z. Li and X. Yang, Evaluation of actuator disk model relative to actuator surface model for predicting utility-scale wind turbine wakes, *Energies* **13**, 3574 (2020).
- [62] X. Yang, S. Kang, and F. Sotiropoulos, Computational study and modeling of turbine spacing effects in infinite aligned wind farms, *Phys. Fluids* **24**, 115107 (2012).
- [63] X. Yang, M. Pakula, and F. Sotiropoulos, Large-Eddy simulation of a utility-scale wind farm in complex terrain, *Appl. Energy* **229**, 767 (2018).
- [64] J. Wiernga, How far can agrometeorological station observations be considered representative? in *Preprint to 23rd American Meteorology Society Conference on Agricultural and Forest Meteorology* (Albuquerque, USA, 1998), pp. 9–12.
- [65] N. Bodini, J. K. Lundquist, and P. Moriarty, Wind plants can impact long-term local atmospheric conditions, *Sci. Rep.* **11**, 22939 (2021).
- [66] X. Ning and D. Wan, Les study of wake meandering in different atmospheric stabilities and its effects on wind turbine aerodynamics, *Sustainability* **11**, 6939 (2019).
- [67] R.-E. Keck, M. de Maré, M. Churchfield, S. Lee, G. Larsen, and H. A. Madsen, On atmospheric stability in the dynamic wake meandering model, *Wind Energy* **17**, 1689 (2014).
- [68] M. Abkar and F. Porté-Agel, Influence of atmospheric stability on wind-turbine wakes: A Large-Eddy simulation study, *Phys. Fluids* **27**, 035104 (2015).
- [69] F. Gustafsson, Determining the initial states in forward-backward filtering, *IEEE Trans. Signal Process.* **44**, 988 (1996).
- [70] V. L. Okulov and J. N. Sørensen, Stability of helical tip vortices in a rotor far wake, *J. Fluid Mech.* **576**, 1 (2007).
- [71] D. Medici and P.-H. Alfredsson, Measurements behind model wind turbines: Further evidence of wake meandering, *Wind Energy* **11**, 211 (2008).
- [72] R. J. Hill, Exact second-order structure-function relationships, *J. Fluid Mech.* **468**, 317 (2002).
- [73] P. A. Davidson and B. R. Pearson, Identifying turbulent energy distributions in real, rather than Fourier, space, *Phys. Rev. Lett.* **95**, 214501 (2005).
- [74] G. Dong, J. Qin, Z. Li, and X. Yang, Characteristics of wind turbine wakes for different blade designs, *J. Fluid Mech.* **965**, A15 (2023).
- [75] S. Kang, X. Yang, and F. Sotiropoulos, On the onset of wake meandering for an axial flow turbine in a turbulent open channel flow, *J. Fluid Mech.* **744**, 376 (2014).